Investigation of photoionization processes in the $3d$-transition metal compounds $FeCl_2$, $FeBr_2$ and $CoCl_2$

DISSERTATION

von

Dipl.-Phys. Mohamed Al-Hada

aus

Sana'a - Jemen

Von der Fakultät II - Mathematik und Naturwissenschaften

der Technischen Universität Berlin

zur Erlangung des akademischen Grades

Doktor der Naturwissenschaften

-Dr. rer. nat.-

genehmigte Dissertation

Berlin-Germany 2005

D83

Investigation of photoionization processes in the $3d$-transition metal compounds $FeCl_2$, $FeBr_2$ and $CoCl_2$

DISSERTATION

submitted to

Mathematics and Natural Sciences Faculty

of the Technical University Berlin

for the degree of

Doctor of Natural Science -Dr. rer. nat-

presented by

Diplom Physicist: Mohamed Al-Hada

born in

Sana'a - Yemen

Berlin-Germany 2005

D83

Promotionsausschuss:

Vorsitzender : Prof. Dr. Erwin Sedlmayr

1. Berichter : Prof. Dr. Peter Zimmermann

2. Berichter : Prof. Dr. Thomas Möller

Tag der wissenschaftlichen Aussprache: 23.11.2005

Abstract

Mohamed Al-Hada

Investigation of photoionization processes in the $3d$-transition metal compounds $FeCl_2$, $FeBr_2$ and $CoCl_2$

In order to have a better understanding of the interplay of intra-atomic and interatomic interaction in the comparison of the molecular spectra with the corresponding atomic on the one hand and with the solid spectra on the other hand, a detailed analysis of the electronic and magnetic structure is absolutely needed. The key of the magnetic and electronic properties of these compound systems are the $3d$ electrons. Analysis of these can be accomplished by exciting $3p$ electrons into $3d$ shell or by a direct exciting of the $3d$ electron. $3p$ photoabsorption spectra of the $FeCl_2$, $FeBr_2$ and $CoCl_2$ show a degree of similarity when compared to the corresponding spectra of the Fe and Co respectively. The comparison of the $3p$ photoelectron spectra of $FeCl_2$, $FeBr_2$ and $CoCl_2$ with the corresponding $3p$ photoelectron spectra of the atomic Fe and Co respectively shows the more distinctive influence of the molecular binding on the valence electron. A further investigation of the influence of the molecular binding on the valence electron was made through the comparison of the $3p$ with $2p$ photoelectron data of the $FeCl_2$.

Contents

List of Figures

List of Tables

Chapter 1

Introduction

The transition metal (TM) compounds $FeCl_2$, $FeBr_2$ and $CoCl_2$ are the systems that have been selected for investigation in this thesis. TM compounds are of importance in many different areas of technology, for example, the magnetic properties of thin films that have lead to a significant improvement in the storage capability of magnetic devices during the last decade. TM compounds are well known for a wide range of physical phenomena [1].

To understand the physics of such complex systems, deep analysis of the electronic and magnetic structure is needed. The key of the magnetic and electronic properties of these compound systems are the $3d$ electrons. Analysis of these can be accomplished by exciting $3p$ electrons into $3d$ shell or by a direct exciting of the $3p$ electron. As such, core hole photoionization is an ideal method to investigate these systems. Production of a core hole can be made through the absorption of incoming light with energy matched to the binding energy of a core electron. This absorption causes the core hole electron to be excited to a bound state or ejected completely from the atom where it becomes a free particle. The production of a core hole by excitation has been studied using absorption spectroscopy and forms the basis for the photoelectron spectroscopy (PES).

Experimental acquisition and the interpretation of photoionization processes in the molecular system is a challenging task. The creation of core holes in molecular

systems is associated with the fragmentation and dissociation processes. In earlier investigations, fragmentation processes of the molecular systems were considered difficult to investigate due to the difficulty of detecting all the fragments produced, making them *terra incognita* [2].

Another difficulty encountered in core hole photoionization processes is the limited number of sources that provide electromagnetic radiation in the Vacuum Ultraviolet (VUV) and soft X-ray region (10 eV -1.5 keV). Standard discharge lamps (e.g. He with 21.2 eV) do not provide emissions over a continuous range of energies and electron guns (in keV range) are not selective excitation sources. With the discovery of the synchrotron radiation (SR) it is now possible to excite with a complete range of energies. Synchrotron Radiation is emitted from relativistic electrons undergoing centripetal acceleration. The introduction of wigglers and undulators installed in storage ring has further improved the radiation source. SR spans the electromagnetic spectrum from infrared to X-rays (more details will be given in section 3.1) and is a valuable excitation source for the study of core hole photoionization processes.

The unique features of the SR have led to rapid growth of research into these sources over the past few decades. At present, more than 25 storage rings for basic and applied research are in operation around the world. The numbers will continue to grow, since several third generation electron storage rings are currently under construction (e.g. Diamond in Didcot (UK), Australian Synchrotron in Melbourne (Australian) and SESAME in Allaan (Jordon)). Recent developments such as the X-ray free electron laser (XFEL) at DESY (Hamburg) will provide users with additional brilliance $10^{33}\ Photon/(mm^2\ mrad^2\ sec\ 0.1\ \%BW)$ reached at photon energies from 200 eV to 12.4 keV.

A first order approximation would be to neglect the correlation effects of a physical system with more than two interactive particles, to provide a sufficient description, but for many systems of interest (e.g. complex compounds) correlations play a major role in their properties. For example, charge transfer effects in transition metal (TM) compounds are caused by the highly correlated ground states

which cause this group of compounds have a complicated structure. The possibility of examining the correlation effects of complex compounds is made relatively simple by studying many electron systems in atomic physics both experimentally and theoretically.

This thesis follows on from the recent, comprehensive investigations of the $3p$ core hole photoionization in $3d$-transition metal atoms by the P. Zimmermann group.

The focus of this thesis is the $3p$ core hole photoionization of evaporated $3d$-transition metal compounds $FeCl_2$, $FeBr_2$ and $CoCl_2$ at temperature of approx. 700 K from stainless steel crucibles. Here, three experimental specific subjects of the $3p$ core level photoionization are focussed upon: photoabsorption spectroscopy, photofragmentation processes and photoelectron spectroscopy. All of these experiments were performed using the SR facility in Berlin (BESSY II).

Using photoabsorption spectroscopy, $3p^{-1}$-$3d$ resonances are studied from partial ion yield spectra of $FeCl_2$ and $FeBr_2$ in the region of the $3p$ (Fe) (50-70 eV). Additionally, $3p$ (Co) in the energy range (50-75 eV) has been studied in the $CoCl_2$ molecule. With photofragmentation processes, the $FeCl_2$ and $FeBr_2$ have been investigated. The main emphasis of this part is on the differences between time-of-flight (TOF) spectral shapes of charged ion Fe^+ from the molecules $FeCl_2$ and $FeBr_2$. For the $3p$ photoelectron spectroscopy of $FeCl_2$, $FeBr_2$ and $CoCl_2$ have been investigated. The aims of this study are to gain a deeper understanding of the influence of the ligand on the molecular binding of the $3d$ valence shell. Corresponding atomic data are good references for the molecular systems. These can be used to analyze the difference between the intra-atomic and inter-atomic effects. Also, corresponding experimental and theoretical solid state data are very useful tools for comparing the molecular spectra in order to predict theoretical models capable of describing experimentally observed complex structure.

This work is structured in the following manner: In the first chapter an introduction displays a general overview of the work. The second chapter deals with the basic theoretical aspects and the basic principles of the molecular dissociation.

Briefly introduction of the charge transfer model of $3d$-transition metal compounds is also presented as a possible interpreting model of the $3p$ photoelectron molecular spectra of the TM compounds $FeCl_2$, $FeBr_2$ and $CoCl_2$. In the third chapter, several experimental techniques for the photoabsorption, photofragmentation and photoelectron spectroscopy are presented. In Chapter four the results of the photoabsorption, photofragmentation and photoelectron investigations of the $3d$-transition metal compounds $FeCl_2$, $FeBr_2$ and $CoCl_2$ are presented. These results are compared to the corresponding photoabsorption spectra of atomic $3p$ Fe and Co as well as to the molecular solid $3p$ spectra $FeCl_2$, $FeBr_2$ and $CoCl_2$. $3p$ $FeCl_2$, $FeBr_2$ and $CoCl_2$ photoelectron spectra are compared to the corresponding photoelectron spectra of $3p$ Fe and Co as well as to the $3p$ solid data. A summary and future directions are presented in the fifth chapter.

Chapter 2

Photoionization Process

2.1 Photoionization Processes

On this thesis, creation and decay of inner-shell vacancies produced in photoionization processes have been studied. The following sections dealing with these processes are based on previous studies in the group of Peter Zimmermann (T. Luhmann, K. Tiedtke, Ch. Gerth and M. Martins).

Photoionization occurs if an atom or a molecule is ionized by the absorption of a photon. In the simplest case, single photoionization of an atom A yield the ejection of an electron and residual photoion A^+

$$h\nu + A \rightarrow A^+ + e^-(\varepsilon\ell) \tag{2.1}$$

in the case, that the photon energy $h\nu$ is larger than the ionization energy E_1. The kinetic energy ε of the emitted electron, due to the energy conservation is given by (Einstein 1905)

$$\varepsilon = E_{exc} = h\nu - E_1 \tag{2.2}$$

where the recoil energy of the ion is neglected [3], since the entire excess energy E_{exc} is carried away by photoelectron due to the large mass ratio between the ion and the photoelectron. Due to an emission of an inner-shell electron in

the photoionization process, a non-radiative (Auger) and a radiative (fluorescence) decayed can lead to singly or multiply charged ions. An inner-shell photoionization process does not only yield the emission of an electron, which rearrange in response to the change of the nuclear shielding produced by the core hole. Thus, inner-shell decay processes reveal complex many body effects due to the correlation of all electrons caused by the electron-electron Coulomb interaction.

The ionization energy E_I (also denoted as the binding energy or ionization threshold) is defined as the difference of energy eigenvalues E_f of the final ionic state and E_i of the initial atomic state,

$$E_I = E_f - E_i. \tag{2.3}$$

Beside the total energy, the total angular momentum and the parity are conserved in the the photoionization process:

$$\overrightarrow{j_A} + \overrightarrow{j_{hv}} = \overrightarrow{j_{A^+}} + \overrightarrow{j_{e-}^+} \tag{2.4}$$

$$P_A \cdot P_{hv} = P_{A^+} \cdot (-1)^\ell \tag{2.5}$$

where $\overrightarrow{j_A}$ and $\overrightarrow{j_{A^+}}$ are the total angular momenta of the atom and the ion, P_A and P_{A^+} are the parities of the atom and the ion, $\overrightarrow{j_{e-}^+} = \overrightarrow{l} + \overrightarrow{s}$ is the angular momentum, $(-1)^\ell$ the parity of the ejected electron for electric dipole transition. $\overrightarrow{j_{hv}} = 1$ and $P_{hv} = 1$ are the momentum and the parity, respectively, related to the photon.

Selected photoionization processes which play a roll in this work are illustrated below:

Single photoionization process is shown in figure 2.1 with the help of an energy level scheme (left hand side) where just an electron participates in the interaction process; the right part of the figure shows the energy distribution of the emitted electrons (photoelectron spectrum). Since the ionization energy ε_{ph} has a definite value that depends on the final ionic state produced, and the photon energy

is usually known, a specific photoionization process can be selected via the kinetic energy of the emitted photoelectrons.

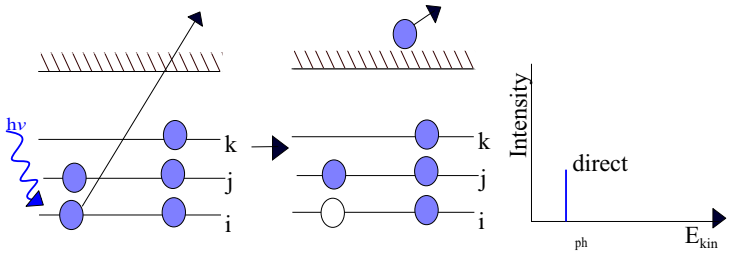

Figure 2.1: Single photoionization process illustrated through the energy level scheme in the left side and the energy distribution of the emitted electrons (photoelectron spectrum) in the right side.

Despite being quite intuitive this model of the single photoionization process is insufficient for the description of the dynamics of the photoionization processes and the correlation of electrons. Taking under account the correlation effects or Coulomb interaction of electrons leads to configuration interaction (CI) to describe the initial state, final state and also intermediate state [4].

In this view other photoionization processes can be described, which give explanation of the diversity in photoelectron spectra lines. These processes are the satellites and Auger processes.

Satellite process has the same procedure of single photoionization but with simultaneous excitation of a second electron (figure 2.2), because in these cases only one electron is emitted and, thus, maxima appear in the energy distribution of the detected electrons at specific energies ε_{ph} and ε_{sat}; these structures are called photoelectron main and satellite lines.

In contrast, in the case of direct double photoionization (DDPI) (figure 2.3), where the second electron is excited into a continuum state, the two electrons must share the excess energy $\varepsilon^{'} + \varepsilon^{"} = E_{exc}$, which leads to a broad continuous energy distribution extending from Zero kinetic energy to E_{exc}.

Auger decay in which an inner-shell vacancy is filled by a non-radiative tran-

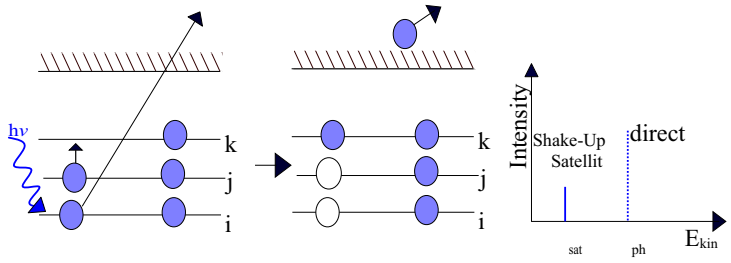

Figure 2.2: Shake-up process showed through the energy level scheme in the left side and schematic photoelectron spectrum in the right side.

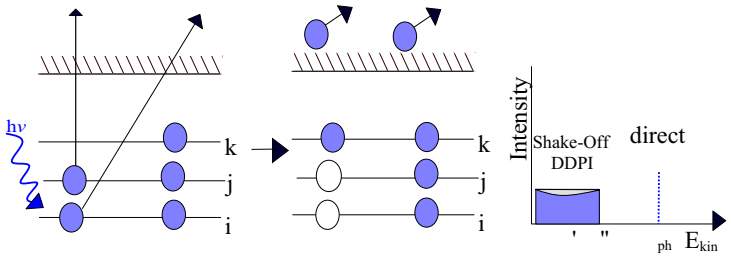

Figure 2.3: Shake-off process pictured through energy level scheme in the left side and schematic photoelectron spectrum in the right side.

sition induced by the Coulomb interaction, is simplified in figure 2.4. Within the two-step model for the photoionization and subsequent Auger decay, the kinetic energy of Auger electrons ε_{Au} is given by the energy difference of the initial $E(i^{-1})$ and final $E(k^{-1}n^{-1})$ ionic state

$$\varepsilon_{Au} = E(i^{-1}) - E(k^{-1}n^{-1}) \tag{2.6}$$

Since the kinetic energy of Auger electrons is determined by the corresponding ion states and independent from the incident photon energy $h\nu$, photoelectrons and Auger electrons can easily be distinguished by changing the photon energy: ε_{ph} varies linearly with $h\nu$, while ε_{Au} remains constant.

Autoionization occurs only at resonance energies $h\nu_{res}$ that correspond to discrete excitation in the atom as depicted in figure 2.5. Here, the excited electron refills the core hole and transfers the energy $h\nu_{res}$ to a valence electron, which is emitted with a fixed kinetic energy

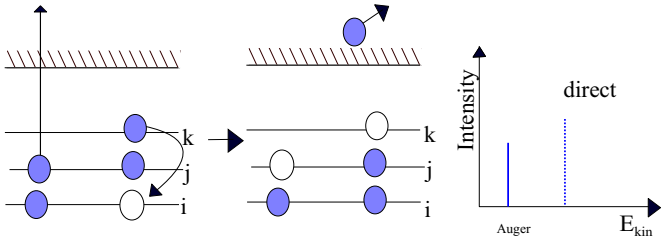

Figure 2.4: Auger decay process presented through energy level scheme in the left side and schematic photoelectron spectrum in the right side.

$$\varepsilon_{au} = h\nu - (E_f - E_i) \tag{2.7}$$

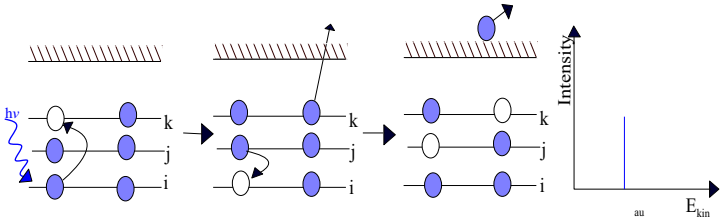

Figure 2.5: Resonant Auger process presented by a two step model through the energy level scheme.

The final state $n^{-1}\ \varepsilon_{au}$ is indistinguishable from the identical state, produced by single photoionization. Quantum mechanically, the indistinguishability of both processes yields interference effects, given rise to asymmetrical resonance profiles (Fano 1961). In the case that the excited electron remains a 'spectator' during the subsequent de-excitation process, the process is called resonant auger process. It is evident that autoionization can not be described properly by a two-step model, since the de-excitation is, in principle, inseparable from the excitation process. The line profile of the autoionization or resonant Auger line is determined by the life time of the core excited state, the monochromator and the analyzer resolution. Due to the fact that there are only two particles in the final state, the emitted electron and ion, it follows from energy conservation that at 'subnatural' linewidths can

be resolved if the experimental bandwidth is narrower than the natural linewidth (Auger resonant Raman effects).

2.2 Many-electron Atoms

The state of a many-electron atoms can be described quantum mechanically by wavefunctions $|\Psi>$ that are solutions of the steady-state Schrödinger equation H $|\Psi>$ = E $|\Psi>$. The energy eigenvalues E can be determined with the aid of spectroscopic methods; whereas the wavefunctions themselves are experimentally unamenable. The exact form of the Hamiltonian depends upon the properties of the system under consideration. The general Hamiltonian of a many electron atom can be written as

$$H = \sum_i H_{k_{int},i} + H_{Nucl,i} + H_{so,i} + \sum_{i \neq k} H_{coul,ik} \tag{2.8}$$

$$H = \sum_i \frac{h^2}{2m}\nabla^2 - \frac{1}{4\pi\varepsilon_0}\frac{Ze^2}{r_i} + \xi_i(r_i)(\overrightarrow{\ell_i} \cdot \overrightarrow{S_i}) + \sum_{i \neq k} \frac{1}{4\pi\varepsilon_0}\frac{e^2}{r_i - r_k} \tag{2.9}$$

Where ∇ is the operator of the kinetic energy and r_i the coordinate of the electron i. $\frac{Ze^2}{r_i}$ describes the Coulomb interaction of the electron i with the nucleus. The last term $\frac{e^2}{r_i - r_k}$ is the interaction of the electron i with all other electrons k in the atom. In equation (2.8) only the spin-orbit operator $H_{so,i}$ as the most important relativistic contribution is included, which describes only the spin-orbit interactions of the electron i and is a single electron operator. In principle the spin and orbital moments of the different electron i and k can also interact. However these two particle interaction (spin-spin, orbital-orbital, spin-other-orbital) are usually much smaller and will not be taken into account in the following. The solution of the first two terms ($H_{kin,i}$, $H_{Nucl,i}$) are simply hydrogenic wavefunctions because here the coordinates of the electrons can be separated. However, the problem is the term $(r_i - r_k)^{-1}$, which describes the direct Coulomb interaction of the electrons. As a result of the Coulomb interaction or correlation term Schrödinger equation would

not deliver exact solutions and being no more analytically solvable, therefore an approximation is required.

Photoionization and electronic structure of the simplest many body problem in atomic physics, the helium atom or helium like ions, can be described almost perfectly by using highly sophisticated theoretical methods ([5] and references therein). Other very intensely studied systems in the gas phase are other rare gases (Ne, Ar, Kr, Xe) due to their closed shell structure [6] [7]. The number of the investigations of open-shell systems which are widely used in applications are relatively limited. Only recently first experimental date on the photoionization has been published for free chlorine [8][9] or bromine [10] atoms. The situation for the important transition metal/compounds is even worse. The lack of information on the photoionization process studies of the 3d transition metals and compounds is huge. This holds for the experimental, where for some atoms or molecules no experimental data and for other atoms or molecules a single measurement exists. In the theoretical side the situation is worse because for most of the $3d$ transition metal atoms and compounds no theoretical studies have been presented [4]. The problem in the case of the transition metals is the open shell character and therefore the huge number of the states and furthermore the strong correlations between these states, which have to be taken into account.

2.2.1 Central-field approximation

In the central-field model the approximation is based on the independent particle model i.e. any given electron (N) moves independently of the others in the electrostatic field of the nucleus and other (N-1) electrons, and to be spherically symmetric. In this model, the state of electrons i is described by a one-electron wavefunction, factorised into radial, angular and spin parts

$$\Phi_i(r_i) = r_i^{-1} P_{n_i l_i}(r_i) Y_{l_i m_i}(\theta_i, \phi_i) \delta_{m s_i}(S_i z) \tag{2.10}$$

where $P_{n_i l_i}(r_i)$ is known as the radial function, $Y_{l_i m_i}(\theta_i, \phi_i)$ is a spherical har-

monic due to the spherical symmetry of the potential. And $\delta_{ms_i}(S_iz)$ represents the spin states. The radial function $P_{n_il_i}(r_i)$ is expected to be a solution of the radial Schrödinger equation (neglecting the spin orbital term)

$$[-\frac{d^2}{d^2r_i}+\frac{\ell_i(l_i+1)}{r_i^2}+V(r_i)]P_{n_il_i}(r_i)=E_iP_{n_il_i}(r_i) \tag{2.11}$$

with

$$E_{av}=\sum_{i=1}^{N}E_i \tag{2.12}$$

Where $V(r_i)$ is the potential of the cental field and E_{av} is the configuration-average energy. The shape of the central field depends on the form of the radial function $P_{n_il_i}(r_i)$ and vice versa; solution for the potential and radial function must be calculated iteratively by a self-consistent numerical procedure, e.g. the Hartree-Fock method, which is outlined below. Since any given electron can be assumed to be moving independently in the field of the nucleus and the remaining (N-1) electrons, a basis function for the entire atom can be written as a product of the one-electron wavefunctions

$$\Psi=\phi_1(r_1)\phi_1(r_1)\phi_1(r_1).....\phi_N(r_N) \tag{2.13}$$

and the set of N pairs of the quantum numbers n_il_i belonging to the one electron functions is called configuration and is written as

$$n_1l_1^Nn_2l_2^{N2}.....n_kl_k^{Nk} \tag{2.14}$$

with

$$\sum_{J=1}^{k}N_j=N \tag{2.15}$$

where the N_j are called subshell occupation numbers.

Pauli principle: the product function dose not reflect the physical indistinguishability of electrons thus disobeying the Pauli exclusion principle (Pauli1925); it is a fundamental postulate that the total wavefunction must be antisymmetric upon interchange of two electrons. Such an antisymmetrical wavefunction can be

constructed from a linear combination of products of one-electron wavefunctions in the form of a determinant and is referred to as a determinantal function or Slater determinant (Slater 1929). This wavefunction is evidently antisymmetric since the interchange of two electron coordinates is equivalent to interchanging two rows, so that the determinant changes sign. The determinant vanishes when two columns or rows are equal, i.e if two electrons have the identical set of quantum numbers $n_i l_i m_i m_{si}$, reflecting the Pauli exclusion principle that two electrons in an atom can not have the same set of four quantum numbers.

2.2.2 Correlation effects

In the independent particle model the Coulomb electron-electron interaction term $(r_i - r_k)^{-1}$ is approximated by the central field. Thus, the many particles Hamiltonian given in equation (2.9) is reduced to an effective one particle problem and the effect of the electron-electron interaction (correlation effects) is only partially taken into account. Already included in the Hartree Fock approximation are multiplet splitting effects and the spin dependent Coulomb exchange interaction due to the Pauli principle. For two identical electrons with the same spin and the same position r_o the many-particle wavefunction has to be $\Psi\overrightarrow{(}r_o) = 0$ following the Pauli principle. Therefore the Coulomb repulsion of equivalent electrons is smaller as compared to non-equivalent electrons resulting in different binding energies.

2.2.3 Hartree-Fock method

The Hartree-Fock (HF) approach is an *ab initio* method for obtaining approximate total wavefunctions for many-electron systems. The method is based on the Central field approximation and the Variational principle. The radial wavefunctions of each subshell are calculated iteratively from the set of HF equations. A set of the radial functions $P_{n_i l_i}(r_i)$ serves as a starting point from which to calculate the mean-field potential. Then the set of HF equations is solved for the radial wavefunction to get a new set of trial functions. This cycle is repeated until satisfactory degree of convergence is obtained. The radial wavefunctions are used to calculate

the configuration-average energy, the Coulomb interaction parameters $F^k(n_i l_i, n_j l_j)$ and $G^k(n_i l_i, n_j l_j)$, and the spin-orbit parameters $\zeta n_j l_j$. The radial integral F^k and G^k are frequently referred to Slater integrals [11] and represent the direct and exchange Coulomb interaction respectively.

In principle, the total wavefunction which is used to describe an atomic state can be expanded in terms of basis functions of any complete set of orthonormal functions. Generally, this set has an infinite numbers, but in practice, only a finite number of basis function can be considered. The simplest choice of a basis is the set of functions that constitute a configuration $(single-configuration\ approximation)$. However, the single-configuration approximation becomes inadequate for the description of an atomic state in such cases where noticeable deviations from the spherical symmetric potential exist. An improvement of the approximation is realized by considering the wavefunction Ψ_b of further configurations, i.e. by an expansion of the set of basis functions. The total wavefunction Ψ^k which describes a stationary state having energy E^k is expanded in term of these basis functions

$$\Psi^k = \sum_{b=1} y_b^k \Psi_b \tag{2.16}$$

where y_b^k reflect the strength of the configuration mixing. The energies E^k will be different from the values that would have been given by a set of single-configuration calculations; this is referred to as configuration interaction perturbation. These two features of wavefunction mixing and energy level perturbation are jointly referred to as configuration interaction.

On this reported work, the atomic spectra Fe and Co beside the molecular spectra of the $FeCl_2$ $FeBr_2$ and $CoCl_2$ are presented. HF calculations using the Cowan code [12] applied for analyzing these atomic spectra. The HF method is often used as the starting point for other more complex methods and has been applied successfully to many areas of quantum mechanics including atomic, molecular and solid-state systems.

2.3 Photodissociation of excited molecules

When a core hole is induced in a molecule by photoabsorption, dissociation is very likely to occur following or even during electronic relaxation, usually yielding molecular ions either with a single -positive charge or double- positive charge. Observation of the molecular or fragment ions produced is informative of the nature of the initially excited or ionized state and of the dynamics of the photofragmentation process. Photodissociation studies provide information about the chemical reaction as well. In chemical reaction investigations the products M and X_2 interact forming an intermediate complex MX_2 that subsequently decays into scattered products, each with different possible properties. However, in photodissociation one starts with the complex as a molecule MX_2 and after absorption of a photon, the formed fragments are detected.

A part of this presented work was focused to investigate the photo fragmentation of $FeCl_2$, $FeBr_2$ and $CoCl_2$ using synchrotron radiation. In contrast to atoms, molecules which are stripped of several outer valence electrons through core excitation, lose their integrity and are efficiently destroyed because many electrons which form the cement of the chemical bonds are removed.

The interest of study core-excited molecules appeared primarily because synchrotron radiation has developed widely throughout the world with more or less routine access to sophisticated beam lines, monochromators, and detection devices. The understanding of photodissociation processes of the singly and doubly charged ions is based on our knowledge of the properties of the molecular orbital. In figure 2.6 a schematic representation of the potential of a diatomic molecule, $A-B$, with occupied and non occupied orbitals. Among outer valence orbitals, 'bonding' orbitals are of special importance because they form the cement of the systems. In contrast, core orbitals are essentially localized on each atomic site and core electrons do not participate in the bonding. The complete description of the dissociation processes in $FeCl_2$, $FeBr_2$ and $CoCl_2$ molecules implies the knowledge of the correlation between the parent molecule's quantum state and the

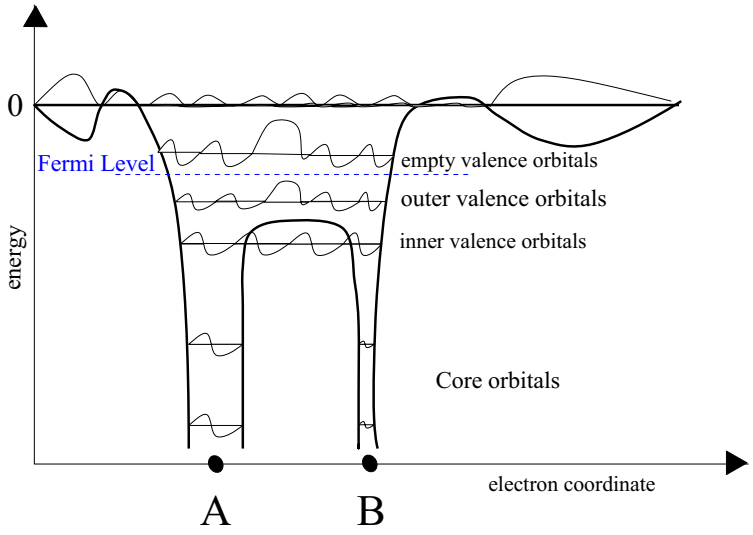

Figure 2.6: Schematic view of the electronic potential in a diatomic molecules. This graphic was taken from [13].

photofragments' quantum state distribution which permits a detailed description of the excited state potential energy surface and frequently provides information about interactions with other electronic states. Due to these specific needs to describe the photodissociation, which is not the main goal of this thesis, we will be restricted our current study to picture the cerated fragments of this process. In addition an investigation on the release kinetic energy of the Fe^+ fragment of the $FeCl_2$ and $FeBr_2$ will be a part of the conducted study in this work.

2.4 Charge transfer model (CT)

According to the success of molding the $2p$ molecular $FeCl_2$ spectrum by a charge transfer model (CT) by Zimmermann and co-workers [14], this is as a result of the close similarity between the $2p$ solid $FeCl_2$ with the corresponding $2p$ molecular $FeCl_2$. The solid $3d^n$ transition metal compounds were interrelated by introducing an additional configuration $3d^{n+1}$. CT model cloud be the most probable theoretical model of the $3p$ photoelectron results in this thesis. Thus, an overview about

the CT model would be here useful to describe.

This section is based on a more recently study done by F. de Groot [15]. He focused of the reasoning behind methods carried out by the groups of Jo and Kotani [16], Gunnarsson and Schönhammer [17], Fujimori and Mnami [18], and Sawatzky and co-workers [19][20][21]. These methods developed the charge transfer model, which based on the Anderson impurity model and related short range model Hamiltonians that were applied to core level spectroscopies.

The occupation of the $3d$-band changes by one as a result of electron transferred from the valence band to the $3d$-band. This $3d^{N+1}$ configuration is affected by multiplet effects, exactly like the original $3d^N$ configuration. $3d^{N+1}$ configuration contains a valence band with a hole. Because the model is used mainly for transition metal compounds, the valence band is in general dominated by the ligand character, for example the oxygen $2p$ valance band in the case of transition metal oxides. Therefor the hole is considered to be on the ligand and is indicated with $\underline{L}$, i.e a ligand hole. The charge transfer effect on the wavefunction is described as $3d^N + 3d^{N+1}\ \underline{L}$ by including the effects of the multiples on the $3d^{N+1}$ $\underline{L}$ a configuration interaction picture is obtained coupling the two sets of multiplet states.

The crystal field multiples for the $3d^7$ and $3d^8\underline{L}$ configurations of Co^{II} are shown in figure 2.7. The $3d^7$ configurations is centered at 0.0 eV and the lowest energy state i the ${}^4T_{1g}$ state, where the small splitting due to the $3d$ spin-orbit coupling were neglected. The lowest state of the $3d^8\underline{L}$ configuration is the ${}^3A_{2g}$ state, which is the ground state of $3d^8$. The center of gravity of the $3d^8$ was set at 2.0 eV, which is identifies with a value of $\underline{\Delta}$ of 2.0 eV. The effective charge transfer energy Δ is defined as the energy difference between states of the $3d^7$ and the $3d^8\underline{L}$ configurations as indicated in the figure 2.7. The effect of charge transfer model is to form a ground state that is combination of $3d^7$ and $3d^8\underline{L}$. The energies of these states were calculated on the right half of the figure. If the hopping parameter t is set equal to zero, both configuration do not mix and the the states of the mixed configuration are exactly equal to $3d^7$ and $3d^8\underline{L}$. Turning on the hopping parameter,

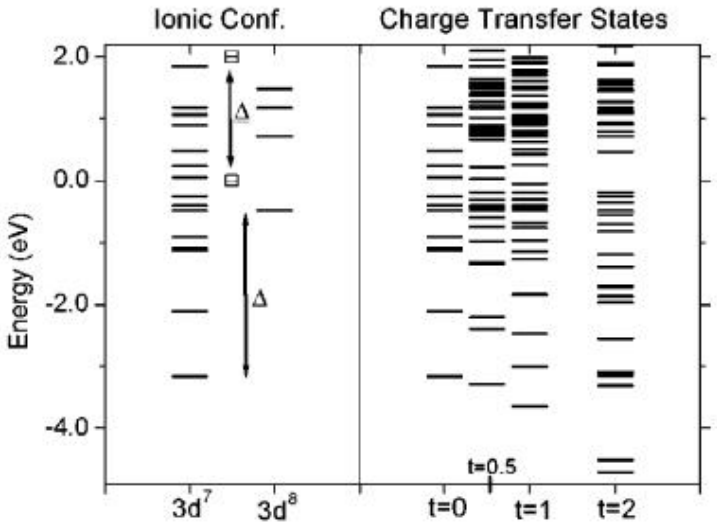

Figure 2.7: Left: The crystal field multiplet states of $3d^7$ and $3d^8$ configurations.$\underline{\Delta}$ was set to $+2.0\ eV$. Right: the charge transfer multiplet calculations for the combination of crystal field multiplet as indicated on the left and with hopping ranging from 0.0 to 2.0 eV as indicted below the states. This figure was taken from [15].

one observes that energy of the lowest configuration is further lowered.

The process on X-ray photoemission (XPS) and X-ray absorption are identical. i.e. the excitation of a core electron from the ground state to some excited state. A difference with X-ray is a difference in measurement. XPS measures the variation in the kinetic energy of the emitted electron at an excitation energy, while XAS measures the variation in the absorption with respect to the excitation energy. The calculated charge transfer multiplet model in the $2p$ XPS spectra is the same model in the$2p$ XAS spectra. The $3d^8 + 3d^9\underline{L}$ ground state is excited to $2p^5 3d^9 + 2p^5 3d^{10}\underline{L}$ in $2p$ XAS and to $2p^8 3d^8\varepsilon_s + 2p^5 3d^9\underline{L}\varepsilon_s$, where ε_s is a free electron. Instead of an ε_s electron, also excitation to a d-electron ε_d are calculated. $2p$ XPS final state involves a real charge transfer effect, in the sense that the state with the lowest energy has a different number of $3d$ electrons in the final state concerning to the initial state. This includes large charge transfer satellites of the calculated $2p$ XPS spectrum of NiO [15]. In the NiO $2p$ XPS it becomes necessary

to include a third configuration $3d^{10}\underline{L}\acute{\underline{L}}$ to the ground state because in the final state it is lowered in energy and mixes the $3d^8$ and $3d^9$ final states. $3p$ XPS follow the same energy scheme as $2p$ XPS. The multiplet effects of the $3p$ and $3s$ core hole are different causing a different spectral shape.

Chapter 3

Experimental Techniques

Many techniques in this chapter were used to study the photoelectron spectra and partial ion yield data following core level photoionization and excitation of the metal halides molecules.

Figure 3.1 shows a schematic illustration of the instruments used in all of the the experiments described in this thesis. This set-up consists of four major parts: the SR facility, the molecular beam, the ion detector (time-of-flight spectrometer) and the electron analyzer (Sienta).

3.1 Synchrotron radiation (SR)

The light source of SR is an indispensable tool to investigate the photoionization process, due to the unique properties of SR which presented in its continuous spectrum, high flux and brightness, high coherence and its wide range of energy from infrared to the X-ray region of several keV.

The first generation of the SR sources has been observed experimentally at General Electric's 70 MeV synchrotron [26] [27] and was described theoretically by Schwinger [28]. The photon flux of the first generation synchrotron radiation was in the range of 100 photons per seconds. Madden and Codling performed their first observations of the absorption spectra of the rare gases in ultraviolet (UVU) region [29]. Dedicated storage rings (second generation of the SR sources)

as BESSY I in Berlin (Germany), or the two National Synchrotron Light Source rings in Brookhaven, NY (USA) were designed and optimized for the usage of synchrotron radiation by circulating an electron or positron beam through bending magnets.

3.2 Third generation light source

A new generation of the storage rings in the 1990's begun their operation, these third generation synchrotron sources such as the European Synchrotron Radiation Facility (ESRF) in Grenoble (France), the Advanced Light Source (ALS) in Berkeley, California, and the *"Berliner Elektronenspeicherring-Gesellschaft für Synchrotron Strahlung "*:Berlin electron storage ring company for synchrotron radiation (BESSY II) in Berlin are characterized by a reduced emittance of the circulating particles beam, and by the extensive use of undulators as radiation sources

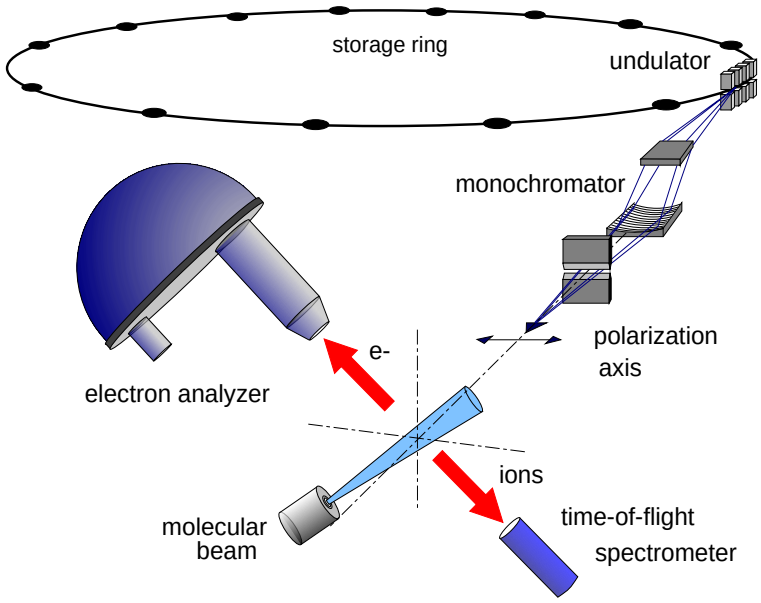

Figure 3.1: Experimental set-up illustrated by four major parts: SR facility at BESSY II (undulator and monochromator), electron analyzer (Sienta 2002), time of flight detector (TOF) and an oven which used to produced molecular vapours

with a further increase of the brilliance by several orders of magnitude. These two properties were the advent of the third generation synchrotron radiation which made the transition from the second generation to it possible.

The improvement of the design and the fabrication of the lattice of magnets that guide the electrons or positrons around the storage have minimized the cross section of the passing particle beam thereby providing incisive brilliance of the radiated photons, which can be expressed quantitatively as the volume of the phase space projection along the horizontal plane of the particle's trajectory, typically of order 5 nm rad in third generation machines in contrast to the order of 30-100 nm rad or more in the second generation rings. The second property is the development of the insertion devices (wiggler, and most importantly undulator) which are aligned in the straight sections of the storage ring. Figure 3.2 illustrate these insertion devices.

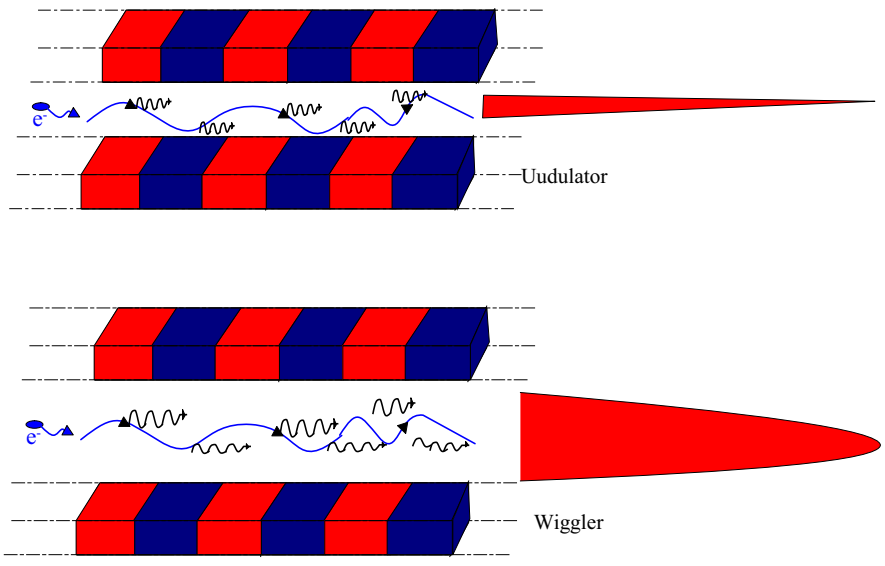

Figure 3.2: Undulator and wiggler

Wigglers are large field devices, which produce deviations of the beam from the straight trajectory, the radiation cones from each bend of the trajectory do not

overlap and the wiggler multiplies the number of bends, preserving the same broad spectrum of emitted wavelength and resulting in an enhanced intensity by a factor N, where N is the number of the magnetic periods. The spectrum of the wigglers is that of a normal bending magnet used in the second generation machine. The undulator is a small field device, where the radiation cones from the whole trajectory of an electron spatially overlap, resulting in a coherence emitted radiation. This enhances the brilliance by a factor of N^2. However, the spectrum is not continuous, but has several sharp peaks, with a width $E/\triangle E = N$ in the first order [30].

3.2.1 BUS Beamline

The overall measurements reported in this thesis were carried out on the undulator U125/SGM-2 at BESSY II in Berlin, which provides the light for the *Berliner Universitätsverbund für Synchrotronstrahlung* (BUS) beamline. Standard undulators contain a periodic array of magnet poles of alternating polarity. The emitted photons in each magnet pole interfere with each other, producing enhanced emission at a fundamental frequency and its harmonics. Due to the quality degradation of the data in many experiments as a reason of the harmonics mixing, higher harmonics are required to be removed. Hashimto and Sasaki [31] [32] proposed an undulatory, which comprises a quasipriodic array of magnet poles called Quasi Periodic Undulator (QPU). Since no rational harmonics but irrational ones are contained in the radiation of the QPU, the light passed through a monochromator without contamination of higher harmonics. From this the U125/2 was constructed as QPU undulator, which never has the regularity in the spectral peaks or harmonics as it offered by the ordinary undulators but a sharp peaks with irrationally factored energies. The spectrum of the (QUP) U125/2 in figure 3.3 illustrates sharp peaks due to the first harmonic E_1 and several higher harmonics E_N. We can see, that the most intense higher harmonics are shifted [31] which has the advantage that these shifted higher harmonics can be eliminated with a Spherical Grating Monochromator (SGM).

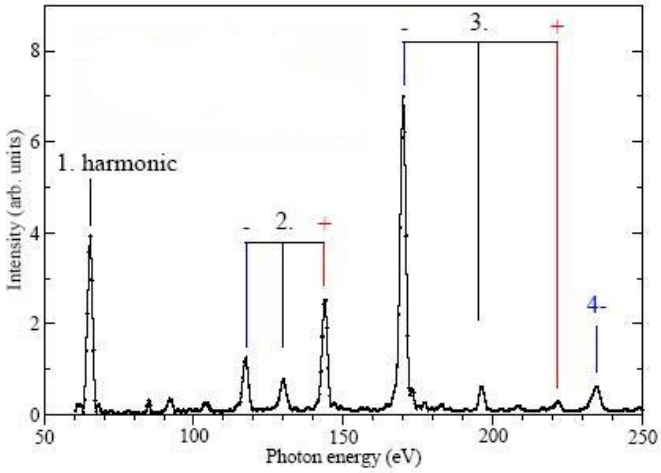

Figure 3.3: Spectrum of the quasi-periodic undulator U125/2 from BESSY II using a gap of 72 mm. The shifted orders are labelled with + and -

.

3.3 Spherical grating monochromator (SGM)

In term of resolution in the third generation SR machines, new beamline constructions were improved to deliver a high resolution with $E/\Delta E > 50\ 000$ [33] [34] [35] [36][37] using either plane-grating monochromators or spherical-grating monochromators. At ALS, a resolution of 1 meV at 64 eV has been achieved by Kaindl et al. [38] [39] by using a dragon type spherical grating monochromator (SGM) at the beamline 9.0.1 (now 10.01). Martins et al. [40] have designed and setup up an XUV undulator beamline (now BUS beamline) for BESSY II, based on a spherical-grating monochromator (SGM). The energy range of the BUS beamline is varying between 29.1-300 eV using the 500 lines/mm grating with 1 meV resolution at 32 eV and by using the 1100 lines/mm grating in the energy ranging between 64.1-250 eV with a 1 meV resolution at 65 eV [41]. A new grating has been aligned and constructed into the monochromator by the BUS-beamline supervisor and the author to serve an energy range from 120-500 eV, while the resolution has not been determined yet. The line polarized light from the BUS beamline has a spot size $70 \times 90\ \mu m$ $(hor. \times vert.)$ and its stability achieved by less than 5 meV.

In this reported thesis $3p$ photoabsorption and photoelectron spectra of the $3d$ metal molecules have been taken in the energy range of 50-80 eV and 100-120 eV respectively using the 500 and 1100 lines/mm gratings. Figure 3.4 shows the flux of both gratings. At the low photon energies, the 500 lines/mm grating delivers higher flux than the 1100 lines/mm grating, but the last is desirable for the high photon energies. $3p$ photoelectron spectra of the $FeCl_2$, $FeBr_2$ and $CoCl_2$ were measured in the energy range 100-120 eV using the 1000 lines/mm, meanwhile photoabsorption (partial ion yield) data were detected using the 500 lines/mm in the energy range of 50-80 eV.

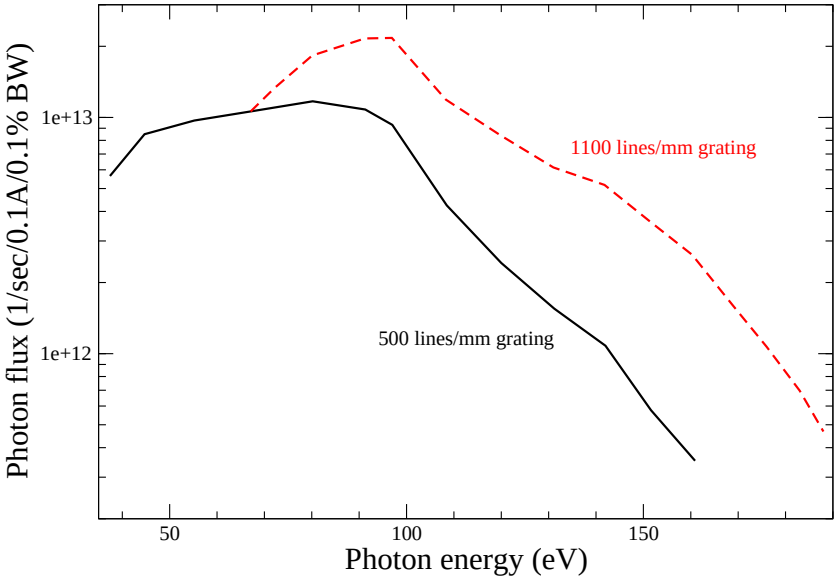

Figure 3.4: Photon flux of the using 1100 lines/mm and 500 lines/mm gratings

The layout of the BUS beamline is presented in figure 3.5; it shows that the undulator radiation is vertically focused by a sagittal focusing cylindrical mirror M_1 onto the entrance slit S_1. This SGM is using the focusing SGM (FSGM) or Padmore design [42] with an additional pre mirror M_2 in front of the grating G. Using this design a moving slit S_2 can be avoided; this is necessary in the Dragon design to fulfill the focusing condition of the spherical grating:

$$(\frac{cos^2\alpha}{\acute{r}} - \frac{cos\alpha}{R}) + (\frac{cos^2\beta}{\acute{r}} - \frac{cos\beta}{R}) = 0 \tag{3.1}$$

where α and β are the angles of incidence and reflection / diffraction, respectively, and $\acute{r}(r)$ the distance entrance slit - grating (exit slit-grating); R stands for the grating radius.

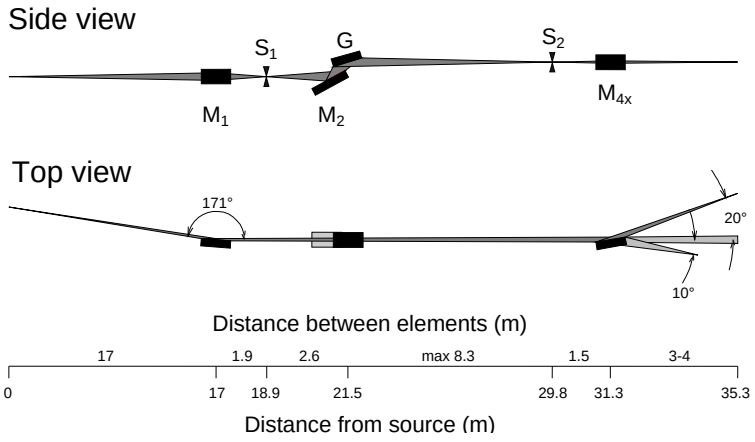

Figure 3.5: Optical layout of the spherical grating monochromator.

The advantage of SGM's is the smaller number of optical elements as compared to plane grating monochromators (PGM). However modern PGM's are somewhat more flexible to operate; thus, they will be operated in the new monochromator beamline for the first XUV-FEL (Free electron laser) at Hasylab/DESY [4]. Peatman [43] offers further description of many monochromators designs and properties.

3.4 Molecular beam technique

In this section a description of one of the important techniques concerning the testing and producing of the targets of the $3d$ metal halides systems that have been reported in this work, at the preparation lab in the TU-Berlin and at BESSY II during the available beamtimes. For a gas-phase experiment on molecules, a sufficient

target density has to be created in the interaction region. There are many methods for producing the molecular beams [44].

In this work, our experiments have been done with an oven as a source chamber in which the vapour pressure is produced by the thermal evaporation of the molecule. The necessary temperature for the vapour pressure inside the oven is taking into consideration by the construction of this source. In the table (3.1) temperatures of the studied molecules are listed for the 10^{-2} mbar vapour pressure, as a typical value for the vapour pressure inside the source chamber and a stainless steel crucible heated by a power in the range of 65 to 75 W. Contrary to the required temperatures of the $3d$ transition metals compounds, the heated power in the $3d$ transition metal atoms covered the range from 80 to 300 W by electron impact of the molybdenum or tantalum crucibles.

Molecule	Temperature (^oC)	Heating power (W)
$FeCl_2$	520	65
$FeBr_2$	515	60
$CoCl_2$	540	75

Table 3.1: Approximate temperatures and applied heating power for the investigated compounds at 10^{-2} mbar vapour pressure molecules [SPD].

Other systems were tested during this thesis, which presented either "an aggressive behavior" of producing the target or a non reaction inside the stainless steel crucible such as $FeCl_3$, $FeBr_3$, FeF_2 and FeI_2. This can explained by the dissociation process and the chemical reactions of these challenging systems, which is reflected on the lack of their evaporation temperatures data in the literature.

Figure 3.6 shows a construction of the used oven to get a sufficient molecular beam target from the grounded stainless steel crucible by heating only the 0.2 mm diameter tungsten wire. The cooling system around the heating region is constructed by an elliptical cooling pipe.

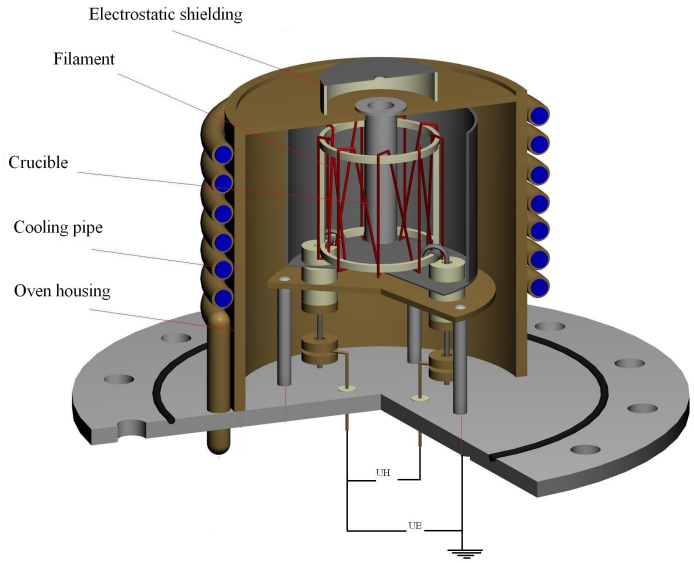

Figure 3.6: A construction of the used oven to get a sufficient molecular beam target from the grounded stainless steel crucible. U_E is generating the needed temperature $\approx 500-600\ ^oC$ whereas the impact voltage U_H set to Zero. The cooling system plays a role to avoid the heated load $\approx 65-75\ W$.

3.5 Photoion spectra technique

Photoion spectroscopy is one of the methods to study the inner-shell photoionization process. In this method ions produced in the decay process subsequent to the excitation are detected. Partial ion yield can be here counted in a time-of-flight (TOF) mass spectrometer. However the photo current (total ion yield) in a simple gas cell can be measured also with this method. In contrast to a simple gas cell, ion yields are accumulated as a function of the TOF mass spectrometer. The ion yield gives the so called mass spectrum distributed into charge states. A mass spectrum can be obtained by an accumulation in this TOF technique, i.e. ions of all species caused by photoionization can be simultaneously detected. Thus, TOF technique is more effective for simultaneous detection for ions of many species [45].

3.5.1 Time-of-Flight (TOF)

In contrast to the magnetic field deflection and quadruple mass filter techniques, time-of-flight (TOF) is one of the recently mass spectrometer techniques in atomic and molecular physics in distinguishing gaseous ions according to their mass/charge ratio. TOF spectrometer combine a relatively simple mechanical setup where ions of all masses can be simultaneously observed with a very high collection efficiency of ions. The principle of the TOF is based on the idea that the velocity of ions depends on the mass/charge ratio under the condition of constant electric field [46]. Mass spectrometer types which are part of recording the ions produced by photoionization except for the TOF have slits to lead ions into the analyzers. However the TOF mass spectrometer without any slit enables basically to take all ions produced by photoionization.

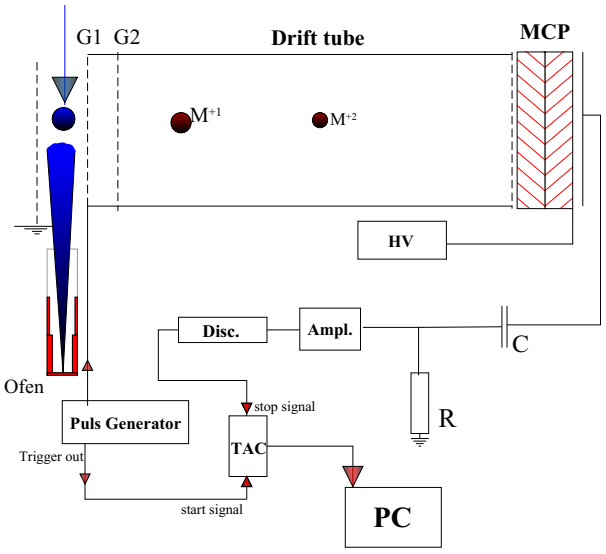

Figure 3.7: A schematic view of the used time-of-flight (TOF) ion mass spectrometer operated in a plus voltage mode. A charged ion hitting the inner wall of the first MCP leads by iterative emission of secondary ions an avalanche of ions. Each MCP amplifiers the signal to the order of 10^3. The signal is collected on the anode. The applied high voltage is $\approx 2.3\ keV$.

The general set up of the TOF is shown in figure 3.7. The design is based

on the Wiley and McLaren instrument [47]. Ions are produced from the vapours of our investigated molecules by the emitted photons from monochromatized synchrotron radiation beamline U125/2 in the ionization section of the TOF. These created ions extracted by the grids G1 and further introduced through G2. The acceleration process of the created ions is done by an electrical extraction pulse mode [48] [49]. Pulses from the pulse generator serve as trigger pulses for a high-voltage (HV) pulse generator and also as start pulses for the time-to-amplitude converter (TAC). Deviating from the original Wiley-McLaren technique, the second acceleration stage is not held at a constant voltage but is pulsed simultaneously with the extraction pulse. G1 and G2 are optimized to increase the mass resolution under the double-field space focusing conditions described by Wiley and McLaren. The resolving power of the TOF spectrometer is given by the greatest mass number M that can be resolved from the neighboring mass number M+1. After acceleration the ions enter into the drift section and are detected by a micro-channel plates (MCP) detector.

3.5.2 Micro-channel plates (MCP)

Channeltrons or micro-channel plates are very convenient detector which have channels acting as continuous dynode electron multiplayer. Channeltron has one channel about 1 mm in diameter, and 50 mm in length with a special shape (a curved channel with a cone at the entrance) while micro-channel plates contains a large number (10^4-10^7) of small channels (10 μm in diameter, 0.5 mm in length) which have a small bias angle (8°) to the input surface of the formed plate. MCP pair is stacked one after the other with opposite bias angles in order to improve the performance. This mounting is called Chevron configuration. For our preparation experiments at the TU-Berlin a channeltron was used, whereas micro-channel plates were applied in our experiments at BESSY II. Figure 3.8 depicts a schematic sketch of the MCP construction. The ions are accelerated into the MCPs by the voltage UMCP. This results in the ejection of electrons from the surface of the MCPs. An electron hitting the inner wall of the first channel plate leads by iter-

ative emission of secondary electron to an avalanche of electrons. The electron avalanche is collected on the anode with short pulses (10 ns) and (20 mV) amplitude, which serve as stop signals for the TOF measurement. The recommended applied high voltages of MCPs was -2.2 kV.

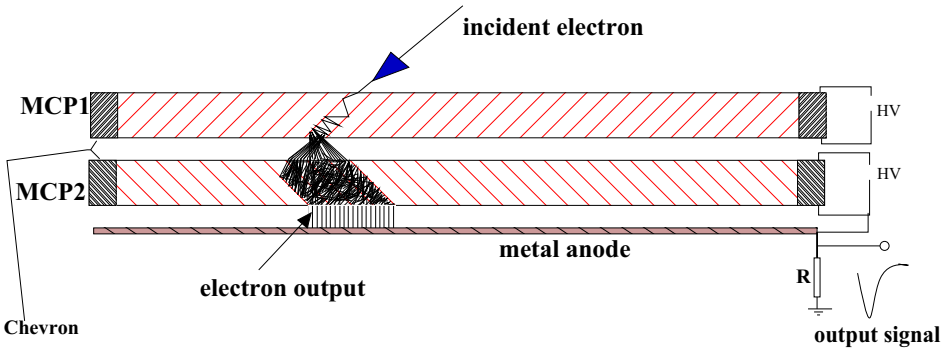

Figure 3.8: An illustration of MCP pair, which are staked together changing their bias angle in a Chevron mounting. This illustration re-sketched from [7].

One of the more significant aspects of the behavior of the micro-channel plates is the saturation effect caused by space-charge limitation. If the charge in the output pulse reaches about 10^8 electrons, the gain can not increase further. The space charge in the output end of the channel repels secondary electrons, causing them to return to the wall without generating further electrons. It is prudent to store the devices in a well desiccated container if they have to be removed from the vacuum environment for longer periods. The devices may be damaged permanently if exposed to gross contamination by hydro-carbon vapours.

3.6 Photoelectron spectra techniques

Precisely what is being done on the basis of the technique of photoelectron spectroscopy is the following: an instrument setup in front of the photoelectron measures its kinetic energy, thereby gaining information about the binding energy of the electron via the photoelectric law. Figure 3.9 shows the principle features of

such an arrangement.

Photoelectron spectroscopy or photoemission spectroscopy (PES) has been established as one of the most important methods to study the electronic structure of molecules, solid state and surface. PES is a method to study the occupied states, where the energy distribution of the emitted photoelectrons is measured and it is assumed that the count rate is proportional to the density of the occupied states [50].

Furthermore, PES has widespread practical implications in various fields, like surface chemistry or material science. In 1981 Siegbahn was awarded the Nobel Prize for his research in the development of high resolution electron spectroscopy for chemical analysis (ESCA).

In the gas phase photoelectron emission depends on the parameters describing the angular distribution of the photoelectron. In general the angular distribution of photoelectrons using a linear polarized light is given by following form:

$$\frac{d\sigma}{d\Omega} = \frac{\sigma_{total}}{4\pi} + (1 + \beta P_2(cos\theta)) \tag{3.2}$$

where $P_2(cos\theta) = \frac{1}{2}(3cos^2\theta - 1)$, σ_{total} is the total cross section, θ is the angle between the direction of the electric field vector of the ionizing light and the emission direction of the photoelectron, β describes the angular distribution of the emitted photoelectron and it can be calculated for an l state (e.g. s, p, d,..) using the Cooper-Zara formula [51]. Neither angular distribution nor cross section been considered in this reported thesis, because photoelectron spectra have been measured with the magic angle (45.7°) using a hemispherical electron analyzer (Sienta SES 2002). Under the magic angle, the term $P_2(cos\theta)$ in the equation 3.2 vanishes and photoelectron emission becomes independent from the β parameters.

3.6.1 Hemispherical analyzer Scienta (SES 2002)

To analyze the kinetic energy, angular distributions, charge ordering, spin ordering and orbital ordering using the photoelectron spectroscopy, high resolution analyz-

ers are favored. In this thesis, electrons kinetic energy being investigated for the probed halide compounds $FeCl_2$, $FeBr_2$ and $CoCl_2$ by using a hemispherical analyzer (Scienta SES 2002).

Due to the low target density in the gas-phase experiments, the resolution is limited in the range of 100 meV. However the hemispherical analyzer Scienta (SES 2002) with 200 mm radius serves a high resolution of 1 meV as the best achieved result.

In figure 3.9 a schematic construction of the electron analyzer SES 2002 is illustrated, it is consists of an electron lens, energy analysis equipment and an electron detector. The electron lens collects the electrons from the sample and focuses them to the entrance of the energy analyzer, producing a photoelectron image of the sample on the entrance plane of the analyzer. Another purpose of the lens is to match the initial kinetic energy of the electrons to the pass energy of the analyzer. Since the analyzer is operating at a fixed pass energy during the acquisition of a spectrum, the chosen energy interval has to be scanned by accelerating or retarding the photoelectron. The energy which that can be recorded is about 10 % of the pass energy E_{pass}.

The electron trajectories are bent in the radial electrostatic field between two concentric hemispheres with a voltage difference ΔV between them. Electrons accelerated in a pathway with a pass radius R_{pass}:

$$R_{pass} = (R_o + R_i)/2$$

and a pass energy E_{pass}:

$$E_{pass} = \frac{e \cdot \Delta V}{\frac{R_o}{R_i} - \frac{R_i}{R_o}}$$

where R_i is the inner sphere radius 160 mm, and R_o the outer sphere radius 240 mm. The separation of the hemispheres is 80 mm. with a standard 40 mm diameter detector.

In front of the detector a field termination mesh is placed which has a two-fold purpose, first it should ensure a homogenous termination of the analyzer field and second it gives a possibility to put a bias voltage on the detector. A small bias

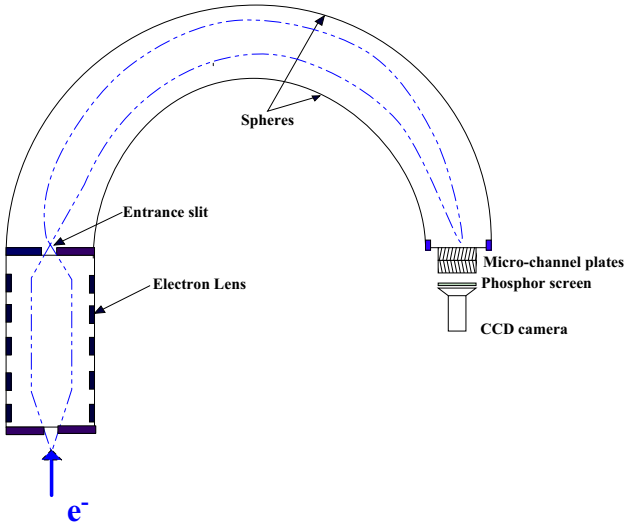

Figure 3.9: A schematic drawing of the electron analyzer SES 2002 showing the principle arrangement for determination of photoelectron energies. A voltage applied between two hemispherical electrodes disperses the electrons with respect to their kinetic energy. The plane of the detector slit is a focal plane and therefore it is possible to use a multichannel plates (MCP's) detector for simultaneous recording of a large part of a spectrum and to study the line shape.

voltage serves to repel low-energy secondary electrons; thus, substantially reducing the background.

When a photoelectron survives to come out the outer side of the space between hemispheres, it strikes at a MCP pair to increase the signal to a more discernible amount. The MCP pair multiplies each incoming electron $\approx 10^6$ times and this electron pulse is accelerated to the phosphor screen, where it produces a light flash. This is subsequently detected by the CCD camera. The position of the light flash corresponds exactly to the position of the incoming electron. It is important that the channels of the first plate are facing the outer hemisphere, since the sensitivity of the plates is much reduced for electrons entering exactly parallel to the channels and electrons tend to imping on the detector with an angle directed towards to the center. In this reported thesis a normal operation mode has been used with a

voltage of about 1850 V for the MCP pair and the acceleration voltage between the last MCP and the phosphor screen was 3800 V.

Chapter 4

Results

The presence of unfilled $3d$ shell has a strong influence on their properties, whose understanding is of considerable interest in order to determine their electronic structure. This has been done experimentally in this present work by exciting - based on the dipole selection rules- $3p$ electrons into the $3d$ shell. In this method the unoccupied $3d$ states will be investigated using photoabsorption experiments. Another way to study the properties of the $3d$ metal halides is the use photoelectron experiments. In this method the $3d$ occupied states will studied by a direct excitation of $3p$ electrons into the $3d$ shell. Both of these methods would be described in detail in this chapter. In addition a part of this chapter will focuse on the produced fragments of the vapour molecule $FeCl_2$, $FeBr_2$ and $CoCl_2$ as a result of the dissociation processes of these transition metal halides.

Recently [52][53] a great interest aroused to investigate the electronic and magnetic structure of the transition metal (TM) compounds systems. TM compounds are well known for their large diversity and richness in physical phenomena [1]. It has been observed that in these magnetic materials a whole wealth of intra-atomic and inter-atomic interactions e.g. charge ordering, spin ordering and orbital ordering are responsible of the properties of these complex compounds [54].

The electronic structure of the seemingly sample transition metal dihalides MX_2 (M= Fe, Co; X= Cl_2 and Br_2) still challenge both experimental and theoreti-

cal scientists. Many vibrational and rotational levels are populated from transition metal dihalides vapours MX_2 molecules. These populated levels result in extremely complex electronic and vibrational-rotation spectra, which are difficult to resolve and to interpret [55]. Furthermore a sufficient molecular beam target of the MX_2 vapours in the interaction region is also one of the main problems in the gas phase experimental studies.

Thus, the probing of $FeCl_2$, $FeBr_2$ and $CoCl_2$ molecules systems in this presented work is a challenging task. This investigation is a very essential study in order to understand the influence of Cl_2 and Br_2 ligands of the probed systems. At the same tim this sort of experimental studies will provide an invaluable guide as what theoretical methods must be applied to gain a correct description and, hence, a deeper understanding and a systematic knowledge of the photoionization process for this sort of molecules. This kind of experiments will be done in this reported thesis using the third generation of synchrotron radiation at BESSY II as an excitation and ionization source on the $3p$ region range of 45-85 eV for the photoabsorption spectra and 100-120 eV for the photoelectron spectra respectively.

4.1 Photoabsorption spectra

The aim of this part is to describe the $3p^{-1} - 3d$ resonances (50-70) eV appearance in the transition metal dihalides $FeCl_2$, $FeBr_2$ and $CoCl_2$. A comparisons study of the probed dihalides molecules spectra with the atomic Fe and Co spectra is presented in this section. The different influence of the ligands (here Cl and Br) will be investigated. The corresponding $3p$ photoabsorption solid state spectra of the $3p$ photoabsorption molecular $FeCl_2$, $FeBr_2$ and $CoCl_2$ will be illustrated. $3p$-photoabsorption resonances in the $3p$ region have attracted the interests of the scientists. Meyer et. al. [56] studied the $3p - 3d$ resonances in photoabsorption and photoemission. They observed that the majority of the observed strong resonances can be attributed to $3p$ transitions into unoccupied $3d$ orbitals i.e. $3p^6 3d^N \rightarrow 3p^5 3d^{N+1}$, with a subsequent emission of a $3d$ electron, i.e.

$3p^5 3d^{N+1} \rightarrow 3p^6 3d^{N-2}\ \varepsilon(p,f)$ as the main decay channel. This is caused by the large overlap of the $3p$ and $3d$ wavefunctions. For a quantitative analysis one has to take into account that the coupling properties of the unfilled $3d$ shells give rise to a large number of discrete states that can interact with a correspondingly large number of continua. In addition the $3d$ and $4s$ orbitals are degenerate in energy resulting in strong configuration interaction of the type $(3d,4s)^N$ with $3d^N, 3d^{N-1}4s$, and $3d^{N-2}4s^2$.

In table 4.1 the evaporation temperature and the ground states of the Fe and Co are shown which are given in the LS coupling scheme.

Element	Temperature (^oC)	Conf.	Intial states	Contribution
Fe	1470	$3d^2 3d^6$	$^5D_{4,3,2,1,0}$	48% , 25%, 15%, 8%, 2%
Co	1540	$4s^2 3d^7$	$^4F_{9/2,\ 7/2,\ 5/2,\ 3/2}$	58%, 24%, 12%, 6%

Table 4.1: Temperature for 10^{-2} mbar vapour pressure and the populated initial states of Fe and Co in the atomic beam.

4.2 $FeCl_2$ and $FeBr_2$

In this part photoabsorption spectra of the $3d$-transition metal dihalides molecules $FeCl_2$ and $FeBr_2$ are investigated. This conducted study focused on a comparison investigation between the molecules $FeCl_2$ and $FeBr_2$ $3p$ photoabsorption spectra and their corresponding data in atomic Fe $3p$ photoabsorption spectra. First, $3p$ photoabsorption spectra of the atomic Fe (experimentally and theoretically) will be presented. Molecular results would be then illustrated and analyzed according to the changeover from atomic to molecule system and also through the different influence of the ligands (here Cl and Br). Eventually the investigated molecule spectra are compared to the corresponding solid spectra.

4.2.1 Fe $3p$ photoion spectra

Experimental results of the partial ion spectrum of singly charged Fe ion in region between 50-70 eV are shown in figure 4.1. The main features in the Fe^{+1} signal are two broad resonance centered at 53.5 and 56.2 eV. These resonances are in a good agreement with the absorption measurements [56].

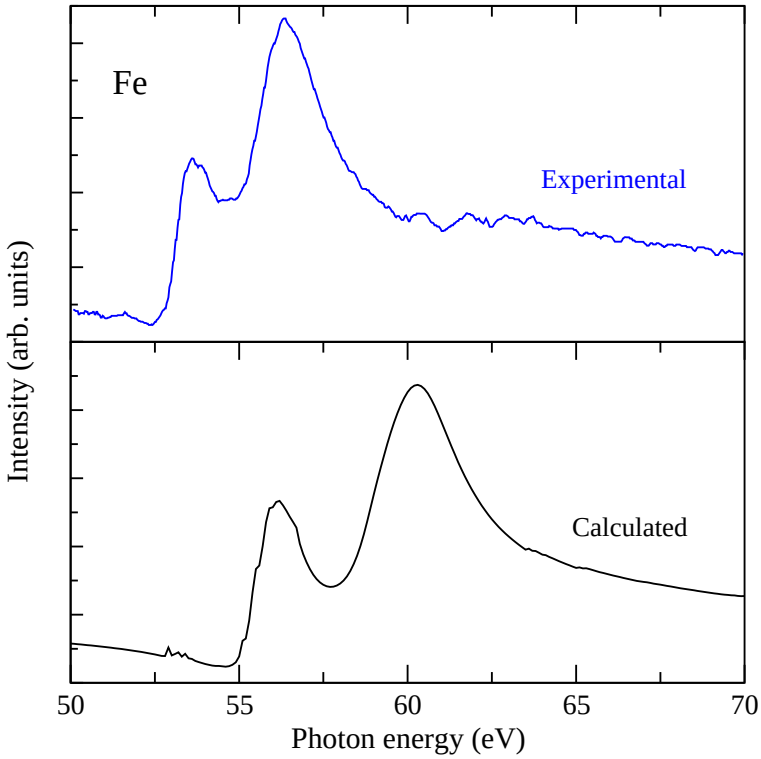

Figure 4.1: Experimental and calculated *Fe* partial ion yield spectra. Upper part: partial ion yield spectra of the atomic Fe in the region of $3p$ excitation and ionization between 50-70 eV. Lower part: calculated cross section for $3d, 4s$ and $3p$ photoionization of the the five initial states $3d^6\ 4s^2\ ^5D$ weighted according to the Boltzmann distribution at the evaporation temperature of 1800 K. [59].

To analyze this signal, calculation procedures have to apply for the $3d$, $4s$, and $3p$ photoionisation cross section in the region of the $3p$ resonances. The calculations were performed in the framework of the Mies formalism [57]. In this formalism the Fano theory of isolated resonances interacting with many continua

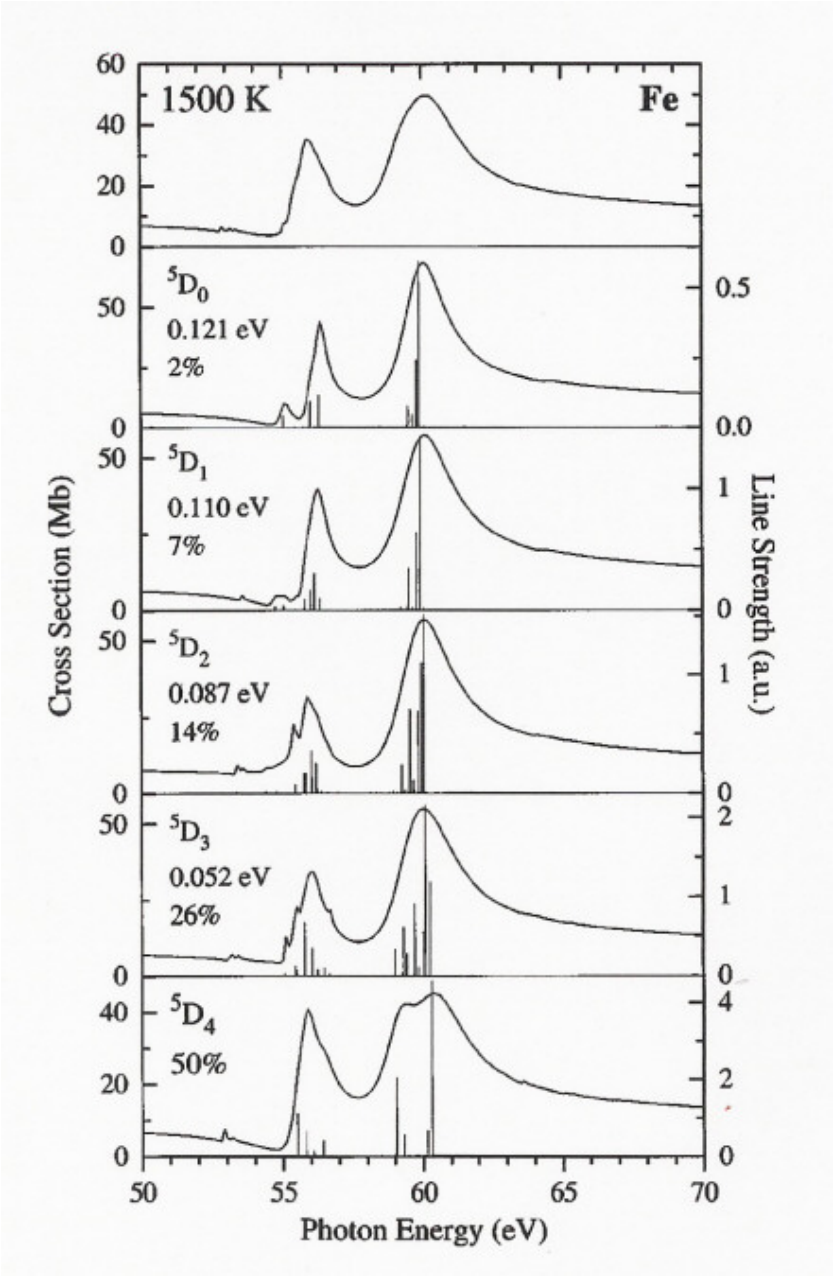

Figure 4.2: Calculated cross section for $3d$, $4s$ and $3p$ photoionization of the five initial states Fe $3d^6\ 4s^2\ ^5D$. The vertical bars represent the line strength of the discrete transitions. The percentage shown is the relative contribution of the respective spectrum to the final *Fe* $3p$ spectrum on the top of the figure [59].

is extended to include the interaction of many resonances with many continua.

Width of a resonance $\Gamma_{n,\beta}$, in the Fano theory, is defined as the sum of all its partial widths into the set of open channels β. When the width of adjacent resonances, however, begins to approach or exceed the spacing, the overlapping of resonances must be considered. For resonances that are coupled to different channels β, their shapes merely superimpose. For resonances that are coupled to the same channels, however, profound interference effects can exist. These effects are introduced by the nonvanishing off diagonal elements of an "overlap matrix" between the continua to which neighboring states are coupled. Configuration interaction of the type $(3d,\ 4s)^N$ was taken into account by the configurations $3p^6 3d^6 4s^2 \leftrightarrow 3p^6 3d^7 4s \leftrightarrow 3p^6 3d^8$ for the initial states and $3p^5 3d^7 4s^2 \leftrightarrow 3p^5 3d^8 4s \leftrightarrow 3p^5 3d^9$ for the excited states. The continua were restricted to the configurations $3p^6(3d,\ 4s)^7 \varepsilon(p,f)$ for the $3d$ and $4s$ ionizations and to $3p^5(3d,4s)^8(s,d)$ for the $3p$ ionization.

The initial states of the Fe were populated in the produced atomic beam at a temperature of about 1800 K. These initial states were classified into five fine structure states $3d^6 4s^2\ ^5D$ (0-0.12 eV)[58]with approximately 50% in the ground state $^5D_4$, 26% in the $^5D_3$, 14% in the $^5D_1$, 7% in $^5D_1$, and 2% in the $^5D_0$.

The calculated photoionization cross sections of these five fine-structure states ^5D_J are shown in figure 4.2. These cross sections are weighted according to their thermal population at 1800 K resulting in the final curve on bottom of figure 4.1 and on the top of the figure 4.2. From a comparison of this final curve with the experimental results in figure 4.1 one can see that the main features with the two broad resonances are well reproduced. Due to the large number of individual resonances, it is impractical to list all transitions; therefore line strengths of the transitions have plotted as vertical bars below the cross sections. The first resonance at the experimental position of 53.5 eV is mainly caused by ^5F transitions and the second resonance at 56.2 eV by ^5P and ^5D transitions. In ref. [56] the ^5P transitions are related to the first resonances. But according to the good agreement here of experimental and theoretical calculations, ^5P and ^5D have the best chance to apply on the second resonances [59]. Because of the configuration mixing of the type $(3d,4s)^N$ similar restrictions as for the LS representation hold for the notation

of the configurations. Nevertheless, one can say that for the ^5F and ^5D transitions the main contributions are due to transitions $3p^63d^64s^2 \rightarrow 3p^53d^74s^2$, whereas for the ^5P transitions strong mixing between $3p^53d^74s^2$ and $3p^53d^84^s$ occurs.

4.2.2 $FeCl_2$ $3p$ photoion spectra

Upper part of figure 4.3 shows the experimental results of the partial photoion spectrum of $3d$-transition metal dihalide $FeCl_2$ in the region of $3p$ excitation between 50-70 eV, meanwhile the lower part illustrates the fit data of the experimental $3p$ of the single charged iron. The sum of fit data has reproduced the main experimental structures by varying the parameters of the fit curve. The parameters used are listed in table 4.2. The main features of the partial ion yield spectra of the single charged Fe^+ has two broad resonances at 54.0 eV and 56.1 eV. These two broad resonances are in a good agreement with the pervious section result of the single charged Fe^+ spectrum. According to the fitted Gaussian function, these two resonances at 54.0 and 56.1 eV were convoluted with the Gaussian profiles of 0.3 and 1.23 eV respectively. In the atomic $3p$ spectra these two resonances are due to the discrete transitions $3p^63d^6 \rightarrow 3p^53d^7$ and a consequent autoionization process to $3p^63d^5 + \varepsilon\ell$.

Postion	Energy position (eV)	Intensity	Gaussian profile
A	54.0	0.37	0.30
B	56.1	0.45	1.23
C	59.0	0.08	1.84

Table 4.2: Parameter values determined by the fit of $3p$ partial photoion spectra of $FeCl_2$ in the excitation region between 50-70 eV.

A close similarity between the photoion molecular spectra of $FeCl_2$ and both calculated and experimental atomic Fe is observed. This suggested that the resonance of the atomic Fe prevail over the influence of the ligand Cl i.e. this dominating behavior of the atomic effects on the inner-shell spectra of the molecules has

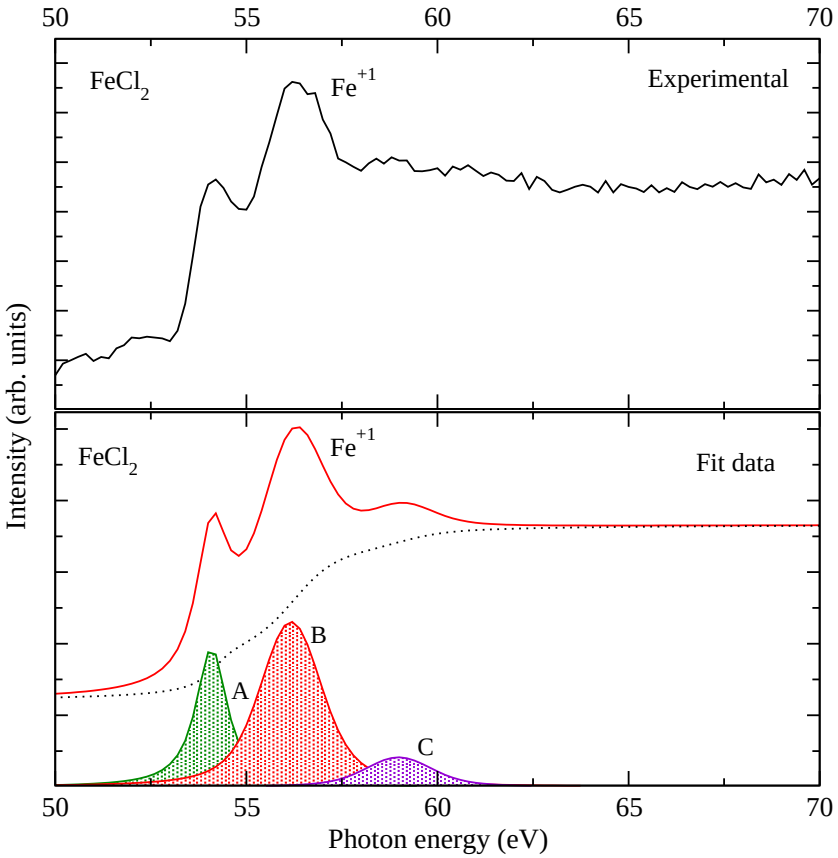

Figure 4.3: Partial ion yield spectra of the molecular $FeCl_2$ and result of the fit data. Upper part: Partial ion yield spectra of the molecule $FeCl_2$ in the region of the $3p$ excitation between 50-70 eV. Lower part: fit data of the experimental result based on the Gaussian distribution of the individual possible peaks as indicated on the bottom of the figure by the lettered A, B and C.

been articulate appeared. The influence of the molecular binding on the valence electrons has presented in the $2p$ photoabsorption atomic Fe spectrum and the corresponding $FeCl_2$ molecular [14] by reducing of the many-body multiplet effects, which affect the spectral shape [61][62] in favor of the spin-orbit doublet. This is related to the $3p$ characterizations in contrast to the $2p$. Since the multiplet effects of a $3p$ core hole are different causing a different spectral shape. This point will discuss more intensively in the photoelectron section.

4.2.3 $FeBr_2$ $3p$ photoion spectra

Figure 4.4 depicted on the upper part the experimental results of the partial ion yield of the transition compound $FeBr_2$ on the $3p$ Fe excitation region (50-70) eV, meanwhile the lower part shows the fitted data of the experimental structures using Gaussian profiles of the main peaks.

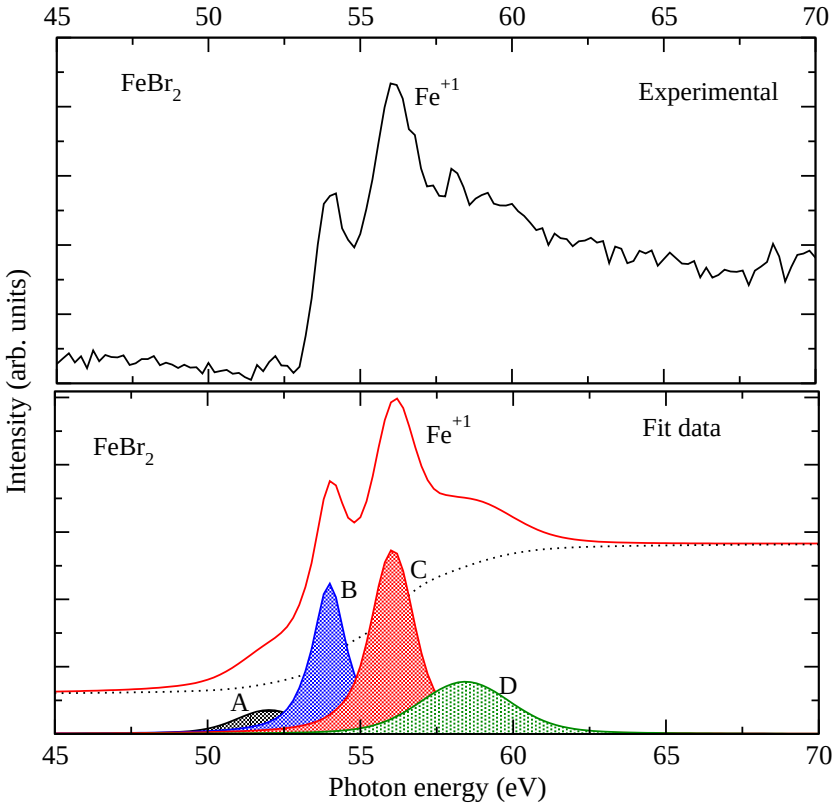

Figure 4.4: Partial ion yield spectra of the molecular $FeBr_2$ and the result of the fitted data. Upper part: partial ion yield spectra of the molecule $FeBr_2$ in the region of Fe $3p$ excitation 50-70 eV. Lower part: fit data of the experimental spectrum based on the Gaussian profiles of the indicated structures as shown on the bottom of the figure by the letters A, B, C and D.

Similar to the $FeCl_2$ partial ion spectrum, the partial photoion yield spectrum of the $FeBr_2$ in the region of 50-70 eV consists of two main resonances centered

at 53.9 and 56.0 eV in a good agrement with the main features of the $3p$ partial ion spectrum $FeCl_2$ located at 54.0 and 56.1 eV. Table 4.3 lists the parameters of the fitted data. The main resonances of $FeBr_2$ were convoluted with the Gaussian profiles of 0.41 and 1.08 eV respectively. In contrast to the $FeCl_2$ system, two small structures at 51.9 and 58.4 eV appear clearly. This might be explained by the influence of the ligand Br which has less electronegativity then the Cl ligands.

Postion	Energy position (eV)	Intnisty	Gaussian profile
A	51.9	0.37	0.065
B	53.9	0.44	0.41
C	56.0	0.53	1.08
D	58.4	0.15	4.67

Table 4.3: Parameter values determined by the fit of the $3p$ partial photoion spectra of $FeCl_2$ in the excitation region between 50-70 eV.

Figure 4.5 shows an overview of the partial photoion yield spectra of the atomic Fe, and the molecular $FeCl_2$ and $FeBr_2$ in the region of the Fe $3p$ excitation (50-70) eV. At the same time the calculated spectrum of the atomic iron and the fitted spectra of the both molecular systems are illustrated.

A similarity has been found here between the molecular $3p$ $FeCl_2$ and $FeBr_2$ photoion spectra with the corresponding spectrum of the atomic Fe. The influence of the ligands Cl and Br are affected in the spectral shape of the single charge ion Fe^+, since the shape of the Fe^+ of $FeBr_2$ molecule differs from that on Fe^+ of $FeCl_2$ molecule in the shoulders. Furthermore it is remarkably that the main resonances in the atomic Fe are broader than those in the molecules. This could belong to the correlation interaction of the Iron with it's ligands (here Cl and Br).

A shifting of the calculated atomic Fe spectrum in the high photon energy direction appears. This shift has been found in the manganese $3p \rightarrow 3d\ ^6P$ giant resonance [63]. The shift in iron, as the subsequent element to manganese, appears as anticipated. This shift has been explained in [4] as a result of including the inter-

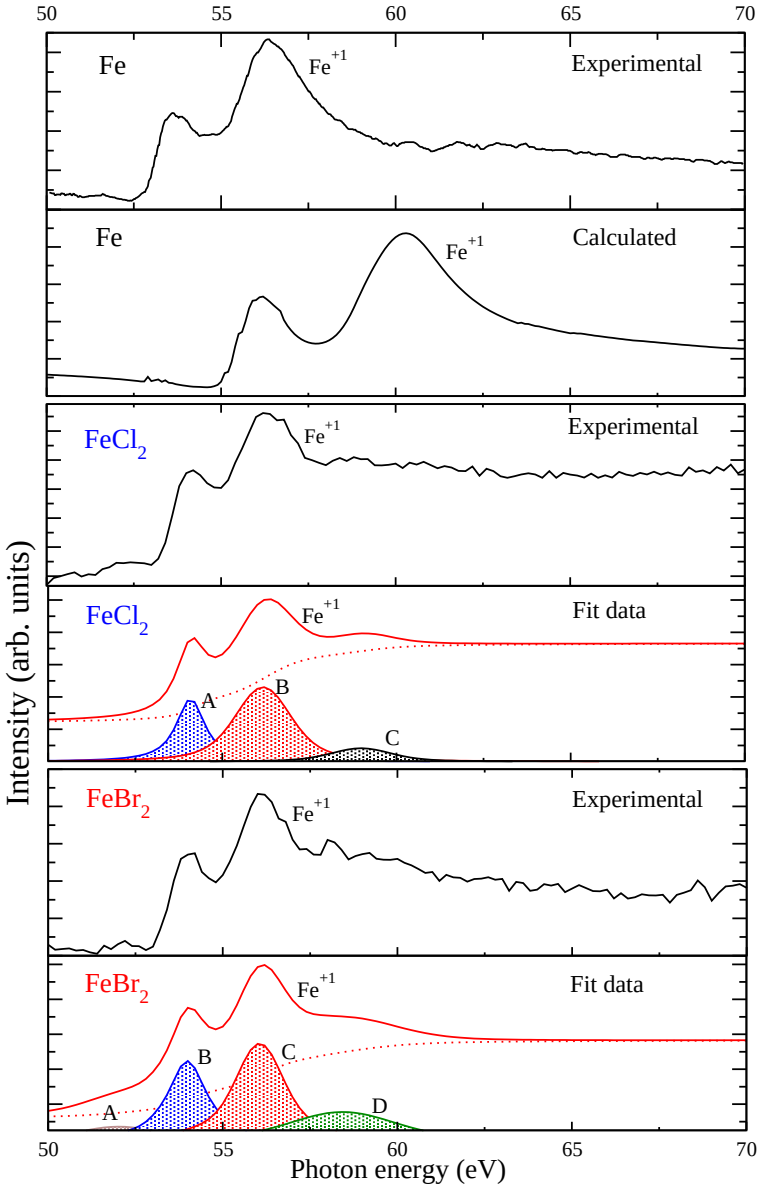

Figure 4.5: Outline of the photoabsorption spectra of atomic *Fe* and molecular $FeCl_2$ and $FeBr_2$. Upper two panels: depicted $3p$ photoabsorption spectra of the atomic *Fe* experimentally and theoretically respectively. Data were taken from [59]. Middle two panels: show $3p$ photoabsorption spectrum of the $FeCl_2$ and it's fitted curve. Lower two panels: illustrate $3p$ photoabsorption spectra of the $FeBr_2$ spectrum and it's fit curve. All spectra presented here are in the region of $3p \rightarrow 3d$ excitation.

action of $3d \rightarrow \varepsilon\ell$ continua in the calculated spectrum. Since the strong interaction with the continuum states causes causes the large shift in the order of several eV for some of the $3p \rightarrow 3d$ resonance positions in Fe [59].

4.2.4 Photofragmentation of $FeCl_2$ and $FeBr_2$

The ion-induced fragmentation of molecules by a photoabsorption process, either below or above a core-ionization threshold leads a dissociation process to appear following or even during electronic relaxation. The pathway to fragmentation is the decay to the core hole, usually yielding molecular ions either with single positive charge (below the threshold) or a double positive charge (above threshold).

In our presented experiment a time-of-flight (TOF) ion mass-spectrometer was used to study the fragmentation dynamics of the positive singly charged Fe fragment ions produced in the $3d$ transition compounds $FeCl_2$ and $FeBr_2$. This experiment has been achieved by using synchrotron radiation -from the BUS beamline at BESSY II- as an excitation source for the Fe $3p \rightarrow 3d$ region by monitoring the yields of the individual ions (partial ion yield).

Studying of the molecular or fragments is informative of the nature of the initially excited or ionized state and of the dynamics of the photofragmentation processes. In addition fragmentation of molecules is of fundamental importance in various areas of science and technology ranging from the physics and chemistry of upper planetary atmospheres to the understanding of radiation damage of biological tissue.

The emphasis here is to study the spectral shape differences incident on the positive singly charged ion fragment Fe^+ from the molecules $FeCl_2$ and $FeBr_2$ in the term of the kinetic energy released E_{kin} during the fragmentation process.

4.2.5 TOF spectra of $FeCl_2$ and $FeBr_2$

The time-of-flight (TOF) experimental results of the vapours $FeCl_2$ and $FeBr_2$ are shown in the upper and lower panels of Figure 4.6 respectively. This spectra were

taken by scanning the photon energy in the region of $Fe\ 3p$ excitation (50-70) eV with a 200 meV step size.

According to the ratio of the mass to charge $\sqrt{\frac{m}{q}}$ the recorded spectrum can distinguish the cerated ions of the probed molecule.

The x-axis of the TOF spectra was converted from channel number values to mass atomic numbers

This mass is given by the formula:

$$\mathrm{M} = (\acute{m}\ \mathrm{ch} + \acute{c})$$

where ch is the channel number of the TOF spectroscopy, $\acute{m}$ and $\acute{c}$ are given by:

$$\acute{m} = \frac{\sqrt{M_2}-\sqrt{M_1}}{Ch_2-Ch_1} \text{ and } \acute{c} = \sqrt{M_1} - \frac{\sqrt{M_2}-\sqrt{M_1}}{Ch_2-Ch_1} * Ch_1$$

where Ch_1 and Ch_2 are the channel numbers of the reference masses M_2 and M_1 respectively.

HOH^+ and N_2 peaks were distinguished here by their masses 28 and 18 atomic mass units (amu) respectively. They were selected as a calibration points of the produced fragments.

The resolution $\triangle t_{TOF}(M)$ can be defined as the difference between the mass number M in amu and the neighboring mass $M+1$ i.e. the time width of the mass peak M is given by:

$$\triangle t_{TOF}(M) \leq t_{TOF}(M+1) - t_{TOF}(M)$$

The recorded ion time-of-flight (TOF) spectra marked in figure 4.6 (upper panel) present the produced molecular and ion fragments of the vapours $FeCl_2$. The intensities of the atomic mass range 30-60 amu and 60-140 amu were scaled up in order to display the produced signals. Cl^{+1} and Fe^{+1} appear at 35 amu and 56 amu respectively, whereas the molecular fragment $FeCl^+$ shows at 92 amu. Weaker peaks located between O_2 and Fe^+ belong to residual gases and impurities or chemical reaction products of the $FeCl_2$. Similar weaker peaks have been observed in the vapours alkali halides salts [64]. Figure 4.6 (lower part) shows the

produced fragments of the vapours $FeBr_2$. As in the upper part the intensities of the atomic masses of the Fe^{+1}, Br^{+} and $FeBr^{+1}$ were scaled up. The residual gases and impurities or chemical reaction products signals are located between O_2 and Fe^{+1} of the $FeBr_2$.

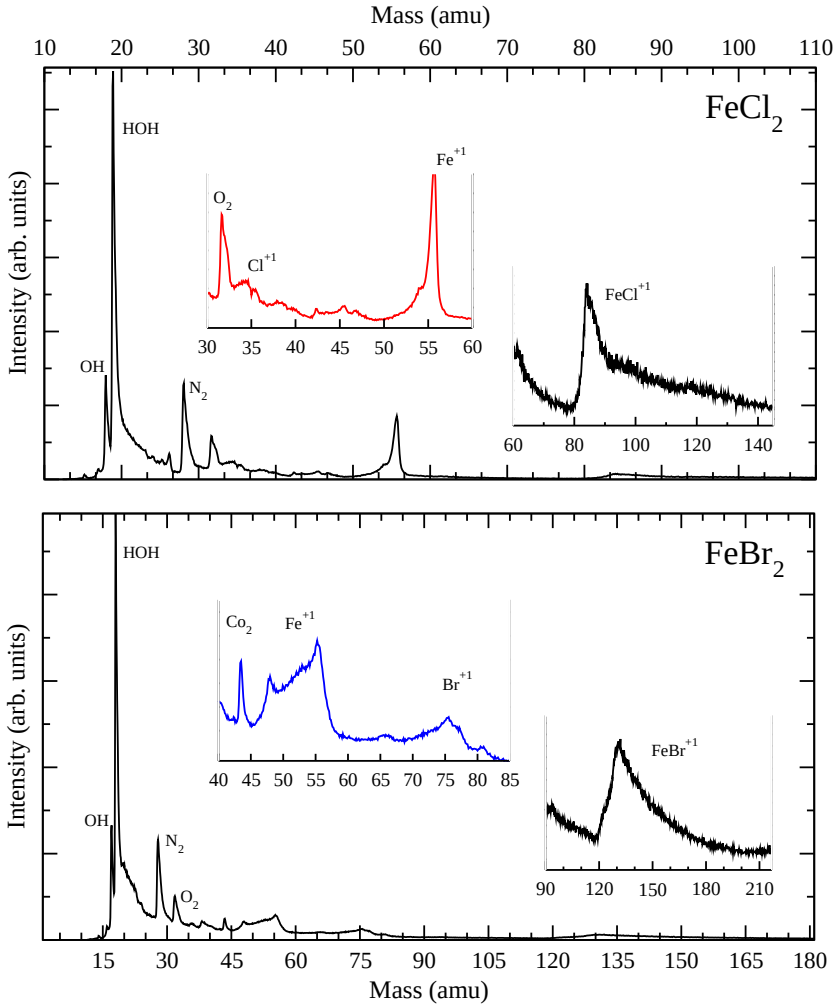

Figure 4.6: Ion time-of-flight (TOF) spectra of $FeCl_2$ (upper panel) and $FeBr_2$ (low panel), measured by scanning photon energy between 50-70 eV

Both the spectra in figure 4.6 at the upper and lower part have been recorded under the same conditions:

- Photon energy covered the Fe $3p$ excitation region 50-70 eV

- TOF techniques
- Measurements period of time

The final result of the core excitation or the ionization processes, which leave the molecule in highly excited states is the production of very unstable ions (singly or multiply charged) which often undergo dissociation [13]. The basic simple question on general rules describing the dissociation process is difficult to answer.

Shapes and widths of the produced ion fragments covered data belongs to the energy distribution [66]. Energy disposal is of prime interest in the field of the molecular reaction dynamics [67][68]. During the dissociation reaction part of the internal energy of the produced fragments is released as kinetic energy E_{KER}.

Earlier measurements in the kinetic energy E_{KER} were mostly involved with the diatomic molecular ions [69][70]. First development in the KER for the dissociation of polyatomics ion molecules has been studied in [71][72]. In this reported experiment, a pules voltage mode signal serves as a start signal, the signal pulse frequency was typically 10 kHz, and signals from the TOF spectrometer detector (MCP) arrive as a stop signal in the time-to-amplitude (TAC) converter. The total distance is x=142 mm [75] and the homogenous electric field applied by two nets was approximately 20 Vcm^{-1}.

In the diatomic Co dissociation and kinetic energy study [73] it was argued that according to [47][74], that the time difference between forward or backward emitted fragments ion is an observable of the kinetic energy release of the dissociation process. An ion emitted in the backward direction will be turned around by the applied electric field. After a time ΔT it turns to its initial position. From then on its further TOF and trajectory are identical to that of an ion with the same kinetic energy initially emitted towards the spectrometer. Therefore in the TOF spectrum ions emitted in the foreword and back word direction will exhibit a time difference equal to ΔT which is probational to the released kinetic energy E_{KER}.

In this work an observation of the produced Fe^{+1} fragment from the vapours $FeCl_2$ and $FeBr_2$ has attracted our interest to study this effect in a first order ap-

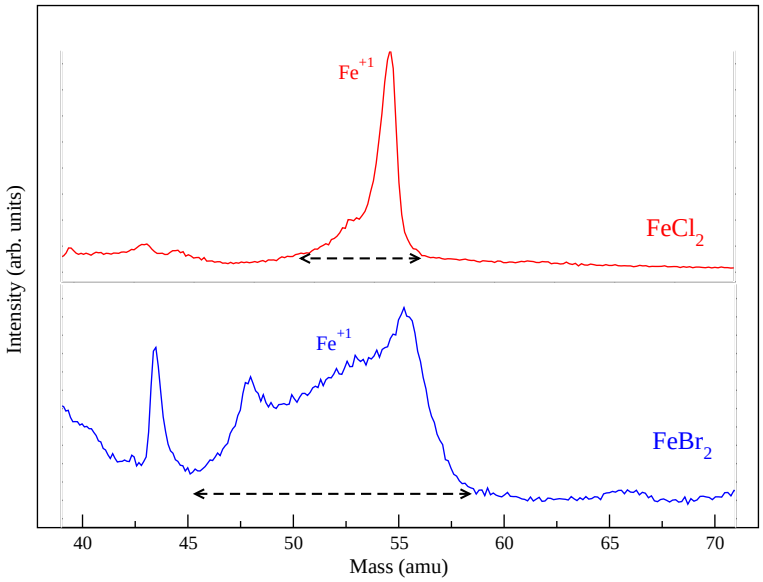

Figure 4.7: Shape broadening of the ion fragment Fe^+ of $FeCl_2$ and $FeBr_2$. Upper part: Ion time-of-flight of the produced ion fragment Fe^+ of the $FeCl_2$. Lower part: Ion time-of-flight of the produced ion fragment Fe^+ of the $FeBr_2$. The spectra were detected by scanning the photon energy in the $3p$ Fe excitation region (50-70) eV.

proximation in term of the kinetic energy released in the molecular fragmentation process. In our work group the photofragmentation mechanism is a *terra incognita* subject. Thus, the inside understanding of this effect would not be easily.

Figure 4.7 illustrates the produced single charged fragments Fe^+ from vapours molecules $FeCl_2$ and $FeBr_2$ on the top and bottom of the figure respectively.

The ion fragment Fe^+ of the $FeBr_2$ system has a broader width then the ion fragment Fe^+ of the $FeCl_2$ system. This would be explicable in term of the fragmentation mechanism. After the bond broken between iron and it's ligand, the kinetic energy E_{kin} will be released . This left over release kinetic energy E_{kin} in the $Fe^+(FeBr_2)$ fragment is much higher than the released ratio of the $Fe^+(FeCl_2)$ fragment. This can be proved by determining the time difference of these fragments.

In the Fe^+ of the molecular $FeCl_2$, two masse were considered in the spectrum

the $M_0 = 55.8$ *amu* in the center of the peak and $M_1 = 52.01$ *amu* the the minimum value at the left of the peak. This yield a time spread ΔT_1 of ≈ 0.35 μsec while the time spread ΔT_2 of the Fe^+ from the $FeBr_2$ molecular is ≈ 1.12 μsec since M_2 and M_o 45.2 and 55.8 amu respectively were treated as broadening parameters in the spectrum. This fact confirmed that the the kinetic energy release from the fragmentation process in the $FeBr_2$ is much more higher than in the $FeCl_2$ molecular.

4.3 $CoCl_2$

Similar to the reported photoion spectra of $FeCl_2$ and $FeBr_2$ molecules spectra, $CoCl_2$ was investigated by the photoion spectra using the TOF techniques to monitor the partial ion yield and synchrotron radiation as an excitation source. The investigated energy range here is the Co $3p$ excitation region between (50-75) eV. First, data of the atomic $3p$ Co will be presented, thereafter molecular data of the measured $CoCl_2$ will be illustrated in order to investigate how Cl ligand influences the molecular system by studying the pure case of the atomic system.

4.3.1 Co $3p$ photoion spectra

The photoion yield spectrum of Co^+ in the region of 50-75 eV is shown in figure 4.8. The main features of the Co^+ signal are three resonances centered at 57.4, 60.6, and 62.7 eV in a good agreement with the results (57.6, 60.4, 62.7 eV) of the absorption results [56].

Like the Fe^+ photoion signal, Co^+ signal has to analyze by the calculation of the $3d$, $4s$, and $3p$ photoionization cross section. Four fine structure states have been populated at the temperature of 1800 K of the initial states. These four fine structure states are presented as following: $3d^7 4s^2\ ^4F(0-0.22\ eV)$ [58] with approximately 59% in the ground state $^4F_{9/2}$, 24% in the $^4F_{7/2}$, 11% in the $^4F_{5/2}$ and 6% in the $^4F_{3/2}$. The continua were restricted to the configurations $3p^6(3d,4s)^8\varepsilon(p,f)$ for the $3d$ and $4s$ ionization and to $3p^5(3d,4s)^9\varepsilon(s,d)$ for the $3p$ ionization. The resonances are due to the discrete transitions $3p^6(3d,4s)^9 \rightarrow$

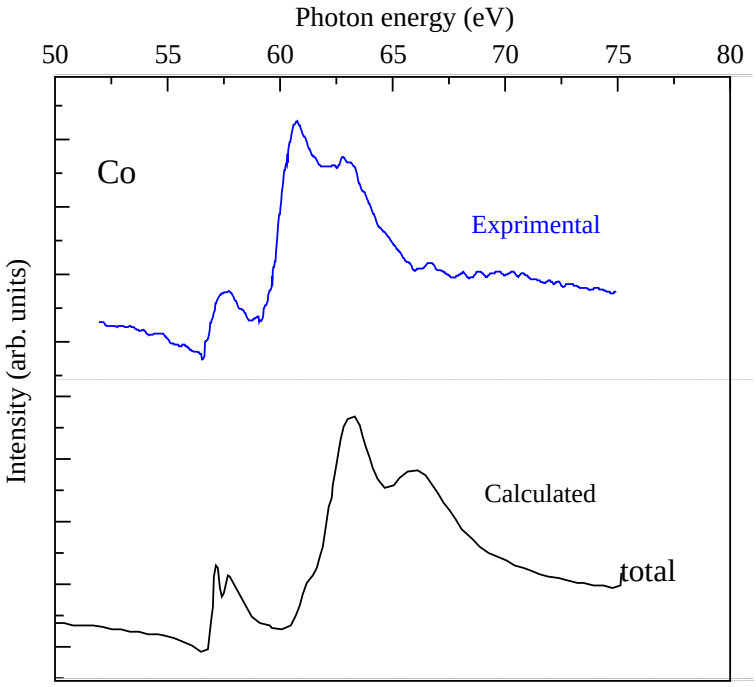

Figure 4.8: *Co* $3p$ photoion spectrum and result of the HF calculation. Upper part: photoion yield spectra of *Co* in the region of the $3p$ *Co* excitation range 50-75 eV. Lower part: calculated cross section for $3d$, $4s$, and $3p$ photoionization of the four fine structure states $^4F_{9/2}$,$^4F_{9/2}$ $^4F_{5/2}$ and $^4F_{3/2}$ populated at 1800 K [59].

$3p^5(3d,4s)^{10}$. Figure 4.9. displays the calculated photoionisation cross sections of the four fine-structure states ^4F_J in the region of 50-75 eV. The individual fine-structure contributions are weighted according to the thermal population at 1800 K with the result of the final curve on top of figure 4.9. The calculated final curve on the top of figure 4.9 shows a good qualitative agreement with the main features of the experimental result on the upper panel of figure 4.8. The resonance at the experimental position of 57.4 eV is mainly caused by ^4G transitions, the resonance at 60.6 eV by ^4F transitions, and the resonance at 62.7 eV by ^4D transitions. The ^4G and ^4F transitions are mainly due to $3p^63d^74s^2 \rightarrow 3p^53d^84s^2$, whereas for the ^4D transitions strong mixing between $3p^53d^84s^2$ and $3p^53d^94s$ occurs.

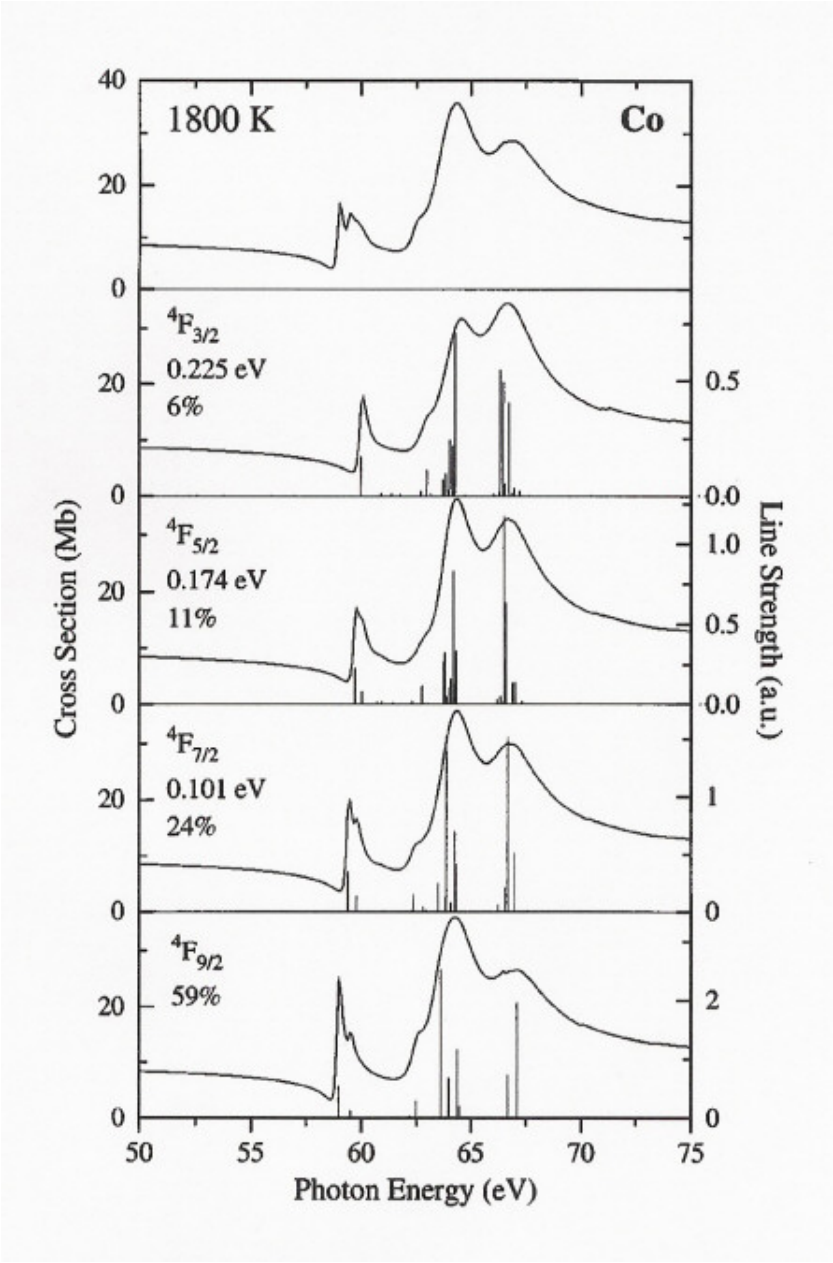

Figure 4.9: Calculated cross section for $3d$,$4s$, and $3p$ photoionization of the four initial states $Co\ 3d^7\ 4s^2\ ^4F$. The vertical bars represent the line strength of discrete transitions. The percentage shown is the relative contribution of the respective spectrum to the final $Co\ 3p$ spectrum on the top of the figure.

4.3.2 $CoCl_2$ $3p$ photoion spectra

The upper panel of figure 4.10 depicts the experimental results of the partial ion yield spectrum of the molecules $3d$-transition metal compound $CoCl_2$ in the region Co $3p$-excitation (50-70 eV). In the lower part fit Gaussian profiles present the possible individual structures of the experimental spectrum labelled by the letters A, B, and C. The sum fit curve on the top of the lower panel reproduces the experimental data in a good agreement. This has been done by varying the parameters of the fit curve which are listed in table 4.4. Thus, as a first order of approximation one can describe the $3p$ Co photoion experimental data in term of the Gaussian distributions of the main experimental structures.

Position	Energy position (eV)	Intnisty	Gaussian profile
A	57.7	0.14	0.36
B	60.9	0.35	0.82
C	62.7	0.17	6.9

Table 4.4: Parameter values determined by the fit of the $3p$ partial photoion spectra of $CoCl_2$ in the excitation region between 50-75 eV.

The main features of the partial ion yield of the $CoCl_2$ system are three resonances centered at 57.7, 62.9 and 62.2 eV in a good agreement with experimental results of atomic data (57.4, 60.6 and 62.7 eV) and to the absorption measurements results (57.6, 60.4 and 62.7 eV) [56]. The responsible transitions of these resonance in the atomic case are: ^4G transitions $(3p^6 3d^7 4s^2 \rightarrow 3p^5 3d^8 4s^2)$ for 57.4 eV resonance, $^4F(3p^6 3d^7 4s^2 \rightarrow 3p^5 3d^8 4s^2)$ transitions for 60.6 eV resonances and ^4D transitions (mixing between $3p^5 3d^8 4s^2 and 3p^5 3d^9 4s$) for to 62.7 eV resonances.

A close similarity between the experimental date of the atomic Co and molecular $CoCl_2$ is seen. Thus, we think that the behavior of the $CoCl_2$ photoabsorption spectra in the $3p$ Co excitation region is identical to the $FeCl_2$ and $FeBr_2$ behavior, concerning their photoion measurements in the Fe $3p$ excitation region, i.e. the atomic Co prevail over the influence of the ligand Cl. Like in the $3p$ photoion spec-

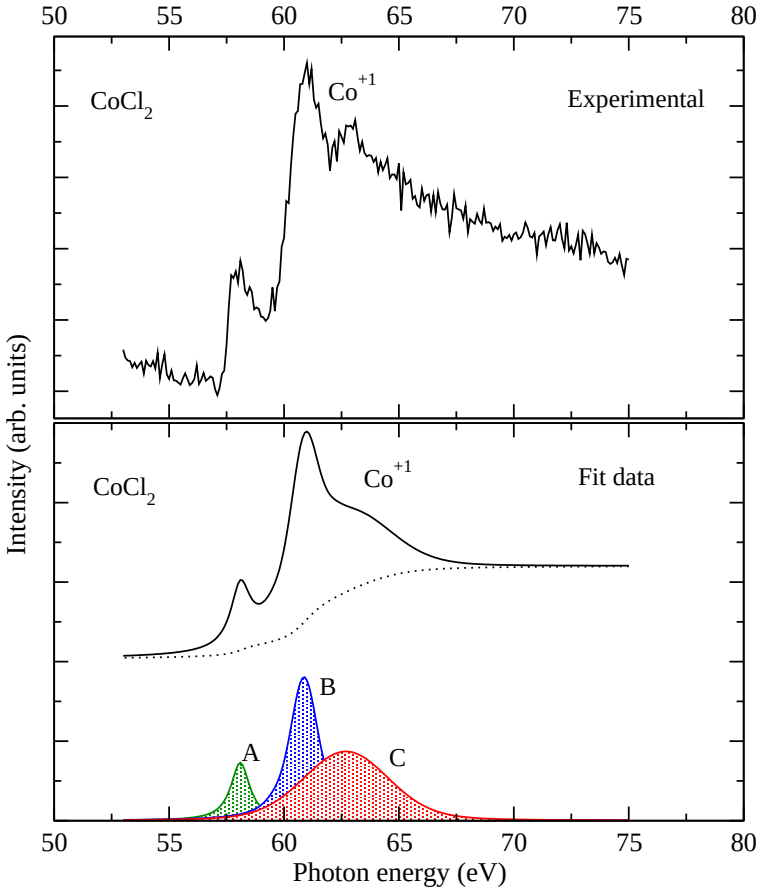

Figure 4.10: Partial ion yield spectra of the molecular $CoCl_2$ and result of the fit data. Upper part: Partial ion yield spectra of the molecule $CoCl_2$ in the region of the $3p$ excitation between 50-75 eV. Lower part: fit data of the experimental result based on the Gaussian distribution of the individual possible peaks as indicated on the bottom of the figure by the lettered A, B and C.

tra of the Fe^+ in $FeCl_2$ and $FeBr_2$, the resonances shape of Co^{+1} in the Co atomic are broader than the corresponding resonance in the $CoCl_2$ molecular spectrum.

4.3.3 TOF spectra of $CoCl_2$

The ratio of the mass to charge $\sqrt{\frac{m}{q}}$, is the key to distinguish the produced charge fragments of $CoCl_2$ molecule. The delivered information in the TOF spectrum are

essential to start the measurements on the $3p$ resonance of the $CoCl_2$ at the Co excitation region (50-75) eV.

Figure 4.11 presents the time-of-flight (TOF) experimental data of evaporated $CoCl_2$ at 700 K from a stainless steel crucible. This data were detected by scanning the photon energy in the region of Co $3p$ excitation (50-75) eV with a 100 meV step size.

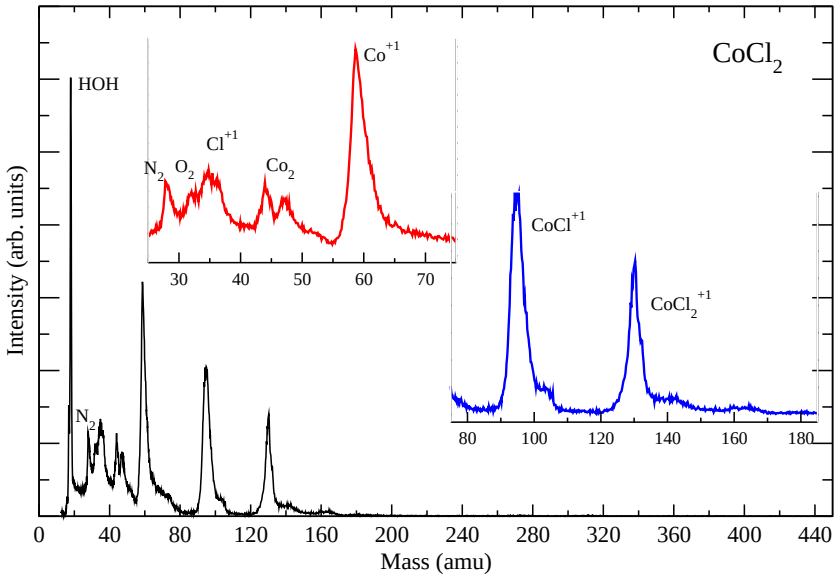

Figure 4.11: Ion time-of-flight (TOF) spectrum of $CoCl_2$ measured by scanning photon energy between 50-75 eV.

By scaling up the intensity of the TOF spectra in the region of 25-75 amu, a dominated signal charge Co^{+1} 60 amu and a structure of the Cl^+ 35 amu are appeared. In addition $CoCl^+$ and $CoCl_2^+$, molecular fragments appear in their mass number positions: 95, 130 amu respectively. Peaks located between the Cl^+ and Co^+ belong to residual gases (e.g. Co_2) and impurities or chemical reaction products of the cobalt dihalide.

4.4 Solid $3p$ photoabsorption spectra of $FeCl_2$, $FeBr_2$ and $CoCl_2$

In this section $3p$ photoabsorption spectra of metal ions of the halides $FeCl_2$, $FeBr_2$ and $CoCl_2$ are compared to the investigated $3p$ photoabsorption spectra of the molecular $FeCl_2$, $FeBr_2$ and $CoCl_2$. Soft X-ray spectroscopy gives important information about the energy-band structures of solids. A common feature of the metal ions of the $FeCl_2$, $FeBr_2$ and $CoCl_2$ systems is that these metal ions have unpaired electrons with the $3d$ shell. Therefore, it is expected that the absorption spectra show many detailed structures associated with the distribution of the empty $3d$ states.

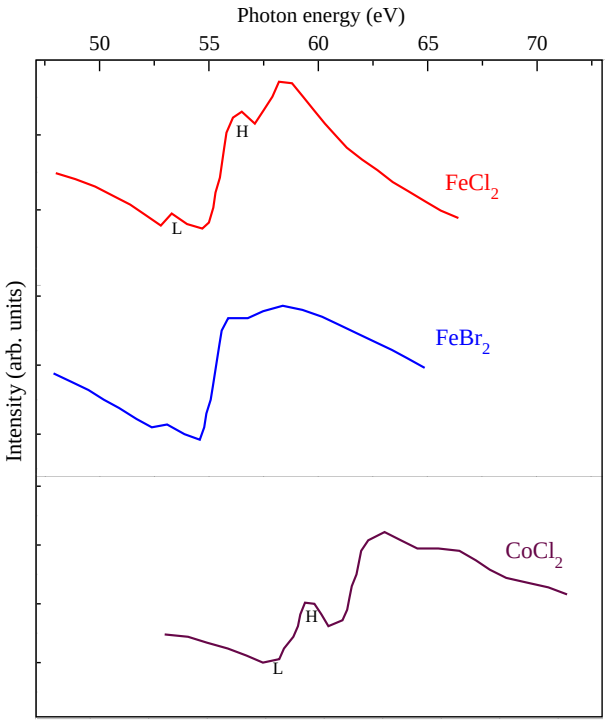

Figure 4.12: Photoabsorption spectra of $FeCl_2$, $FeBr_2$ and $CoCl2$ in the solid state taken from [76]. The first peak of the low energy structures in $FeCl_2$ and $CoCl2$ indicted by L and that of the high energy structures shown by H.

The structures here are classified into two groups: a rather weak and narrow

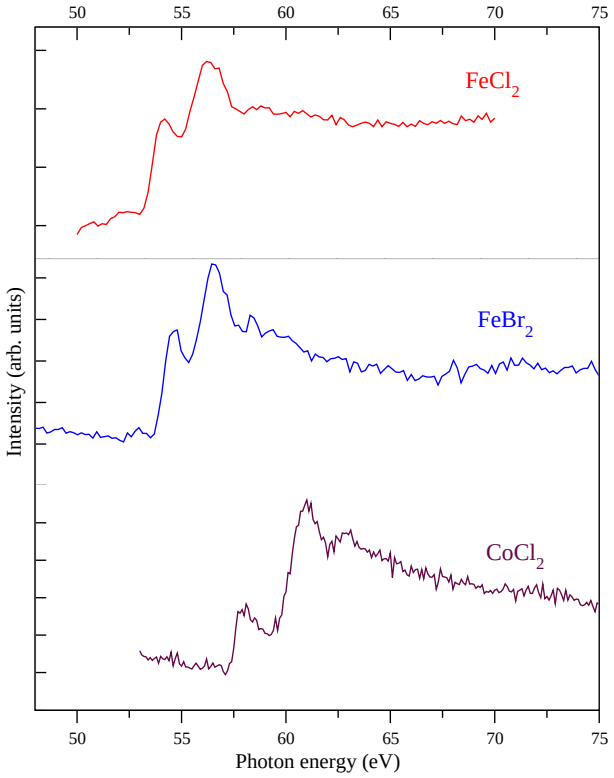

Figure 4.13: Molecular $FeCl_2$, $FeBr_2$ and $CoCl_2$ photoabsorption spectra in the $3p-3d$ excitation.

band occurring in the low-energy side of the absorption threshold and the other consists of an intense and rather broad band appearing in the high-energy side of the threshold. By comparing our data of the $3p$ $FeCl_2$ $FeBr_2$ and $CoCl_2$ photoabsorption spectra (figure 4.13) with the corresponding solid spectra (figure 4.12), one observes a close similarity at the main structures. This fact suggests that the $3d$ orbital in the molecular $FeCl_2$ $FeBr_2$ and $CoCl_2$ spectra are localized. The energy separation in the metal spectra between the first peak of the low-energy structure (labelled by L) and that of the high-energy structure (shown by H) becomes smaller with the order of $FeCl_2$ and $CoCl_2$. This may suggest that the separation between the empty $3d$ states and $4s$ band of these systems becomes smaller with this order. This effect has been noted in the molecular $FeCl_2$ and $CoCl_2$ spectra.

It has been suggested that the narrow absorption profiles of each of the low

energy structure belong to the small wavefunction of the 3d states which overlap with the nearest neighbor ions; thus, the 3d states are well localized states in the transition halides.

4.5 Photoelectron spectra

In this section direct $3p$ photoemission experiments on $3d$-transition metal compounds $FeCl_2$, $FeBr_2$ and $CoCl_2$ are presented. Contrary to the photoion spectroscopy signal, which integrates over all final states and recorded with 4π acceptance, the photoemission experiments partial, angularly resolved cross sections are measured with a limited acceptance. Thus, the measured count rate in the photoemission experiments will be several magnitudes smaller than for those in the photoion spectroscopy. This is one of the difficulties to carry out the photoemission experiments using the low target densities of the molecular vapour beams. The recent development of the COLTRIMS technique (Cold Target Recoil Ion Momentum Spectroscopy) provides a coincident multi-fragment imaging technique for eV and sub-eV fragment detection. In this technique electron spectra can be measured with 4π acceptance [83] [84]. This technique is performed and designed for the cold atomic target, and would be therefore not easily to apply it for the free metal molecules.

The facing challenge in analyzing the measured compounds is to distinguish between the intra-atomic multiplet splitting and interatomic effects (charge transfer (CT), ligand field splitting). The nature of the satellites for the case of $2p$ photoemission of the solid MnO [77][78] [79] has been recently controversially discussed. Bagus et. al. [78] assigned the satellites structures in MnO to an inter-atomic inter-shell $(2p, 3d)$ many-body effect due to a valence shell recoupling in MnO using an *ab initio* Dirac Fock (DF) calculation. Whereas Kotaine and coworkers explained in earlier papers [81] [82] from a multiplet calculation including solid state effects, that the CT plays also an important role. Nevertheless, Begus et. al. [77] and Taguchi et. al. [79] agreed that atomic many body effects account for the most of the features in the MnO $2p$ and $3p$ photoemission spectra.

In the following attention will be focused on a comparison study of the $3p$ photoelectron spectra in the $FeCl_2$, $FeBr_2$ and $CoCl_2$ transition compounds with the corresponding data of the atomic Fe , since data of the later are informative

to study the influence of the inter-atomic interplay in the *Fe* and *Co* dihalides like $FeCl_2$, $FeBr_2$ and $CoCl_2$. In addition correlative X-ray photoemission spectra (XPS) from $3d$-transition metal $3p$ and $2p$ core levels in $FeCl_2$ and $CoCl_2$ compounds will presented. According to the similarity of the $2p$ molecular $FeCl_2$ spectrum [80] with the corresponding spectra in the solid [81]. $2p$ photoemission spectrum of the molecular $FeCl_2$ has been analyzed using the same model, which explains the solid structure. The modelling is based on the charge transfer model and introduces an additional $3d^7$ configuration.

4.6 $FeCl_2$ and $FeBr_2$

$3p$ photoemission spectra of the $3d$ transition metal compounds $FeCl_2$ and $FeBr_2$ are presented in this section. Production of a sufficient beam target into the interaction region is accompanied by the dissociation processes of the Cl_2 and Br_2. Thus, this step in our experiment is a delicate process to probe these kind of molecule systems.

First, $3p$ photoemission *Fe* spectra will be demonstrated experimentally and theoretically, thereafter $3p$ photoemission $FeCl_2$ and $FeBr_2$ are presented, since the interaction of *Fe* $(3p)$ hole with the $3d$ valence electrons can be also used to study the influence of the molecular binding on the $3d$ valence shell in compounds systems $FeCl_2$ and $FeBr_2$.

4.6.1 $3p$ photoelectron spectra of atomic Fe

Figure 4.14 (a) displays the experimental $3p$-photoelectron spectra [85]. This spectra were recorded at a photon energy of 127 eV with a 700 meV resolution. Due to the huge two particles $3p-3d$ Coulomb interaction, $3p$ spectra covered an energy range of 20 eV.

In the energy range between 63 eV and 85 eV several structures (labelled A-H) were observed.

The lines in the low energy region of *Fe* been analyzed using a high resolution

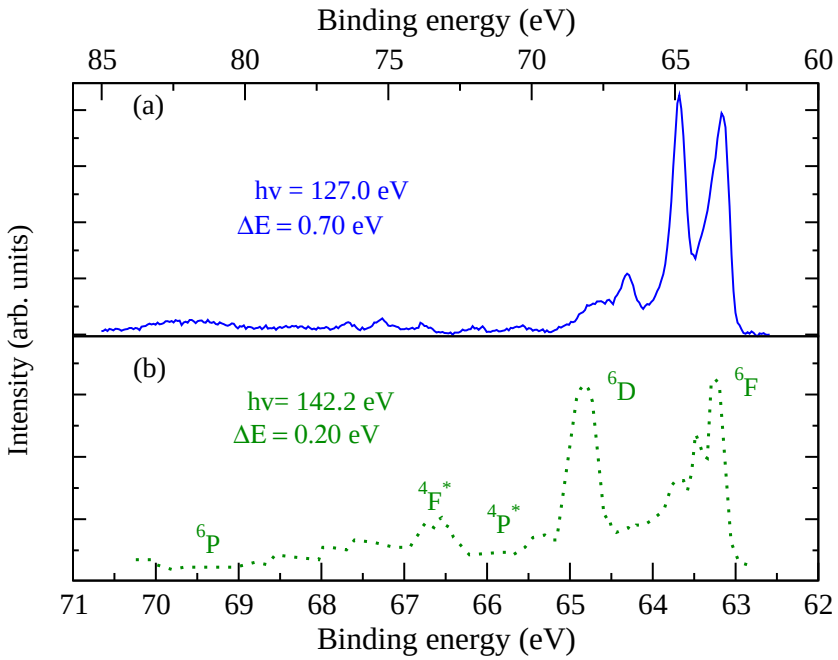

Figure 4.14: *Fe* $3p$ high resolution photon electron spectrum and results of HF Calculation in the high energy region taken from [87]. Upper panel: experimental $3p$ photoelectron spectrum of the atomic Fe taken at 127 eV. Lower panel: high resolution in photoelectron spectrum $\triangle E = 200$ *meV* of *Fe* recorded at photon energy of 142.2 eV. Note the different in the energy scale.

photoelectron spectroscopy 200 meV recorded at 142.2 eV [87]. This is shown in figure 4.14 (b). Hartree Fock (HF) calculations were applied using the Cowan code [12]. The initial configurations $3d^6 4s^2, 3d^7 4s$ and $3d^8$ and the final configurations $3p^5 3d^6 4s^2\ \varepsilon(s,d)$, $3p^5 3d^7 4s \varepsilon(s,d)$, and $3p^5 3d^8\ \varepsilon(s,d)$ were taken into account.

The structures in the *Fe* spectra figure 4.14 (a) can be classified into two line groups: high spin component ${}^6L$ and low spin components ${}^4L$ ($L = P,\ D,\ F$). The high spin states ${}^6L$ can only be formed by coupling the $3p^5\ {}^2P$ core hole states to the $3d^6\ {}^5D$ states, while the low spin states ${}^4L$ can originate from a coupling of the $3p^5\ {}^2P$ vacancy with $3d^6\ {}^5D$ states as well as with $3d^6\ {}^3L^*$ satellite states, where the asterisk indicates a re-coupling of the $3d$ shell. The $3p^{-1}$ multiplet structure thus can be classified into tow binding energy regions: low binding energy and

high binding energy. The low binding energy dominated by the high spin states ^6L, whereas the low binding energy region is covered by $3p^5 3d^6$ (^5D) states. The comparison of the calculated to the experimental structures of the atomic Fe in the bottom of figure 4.14 presents two dominated photoelectron lines based on the result of HF calculation. These two main lines can be assigned to the final ionic states ^6F and ^6D.

The ^6F multiplet at 63.4 $\pm$ 0.2 eV is in good agreement with the $3p^{-1}$ threshold energy of 63.4 $\pm$ 0.5 eV estimated from $M_{2,3}$ Auger spectra [86]. The other photoline multiplet at a binding energy of 64.8$\pm$ 0.2 eV refers to the ^6D multiplet.

According to the calculations the weak shoulder apparent at the binding energy side originate from the $^6D_{9/2}$ state, which is found to be separated from the states $^6D_{7/2}$ - $^6D_{1/2}$ by 0.2 eV. The structures of the small peaks at 65.4 eV and 65.9 eV could be due to $^4P^*$ satellite states.

The experimental spectrum at the high binding energy shows a broad band which probably comprises the predict lines $^4F^*$ and ^6P by the calculations. In addition to the behavior of the structures in the high energy region, the experimental spectrum dose not show any marked structure at the energy calculated for the ^6P states.

The understanding of the experimental spectrum at the high binding energy (low spin region) has been investigated by K. Tiedtke et. al. [85]. They studied the life time broadening in the $3p$ photoelectron spectra of atomic Fe at 127 eV. The broadening in these photolines can be explained by the term-dependent transition probabilities of the subsequent Auger decay as it was calculated by McGuire [88]. The reason lies in the strong dependence of super-Coster-Kronig SCK decay $3p^5 3d^6 \rightarrow 3p^6 3d^4 \varepsilon\ell$ on the total spin S. This decay favors the low spin components ^4L in comparison to the high spin components ^6L. The effect of the Auger transition probabilities in the $3p^{-1}$ multiplet is shown in figure 4.15 (b) and (c). In part (b) of the figure 4.15 the calculations do not consider the subsequent Auger decay, whereas the calculated spectrum in the part (c) includes the subsequent Auger decay. It is clear that by the life time broadening of the low spin components the

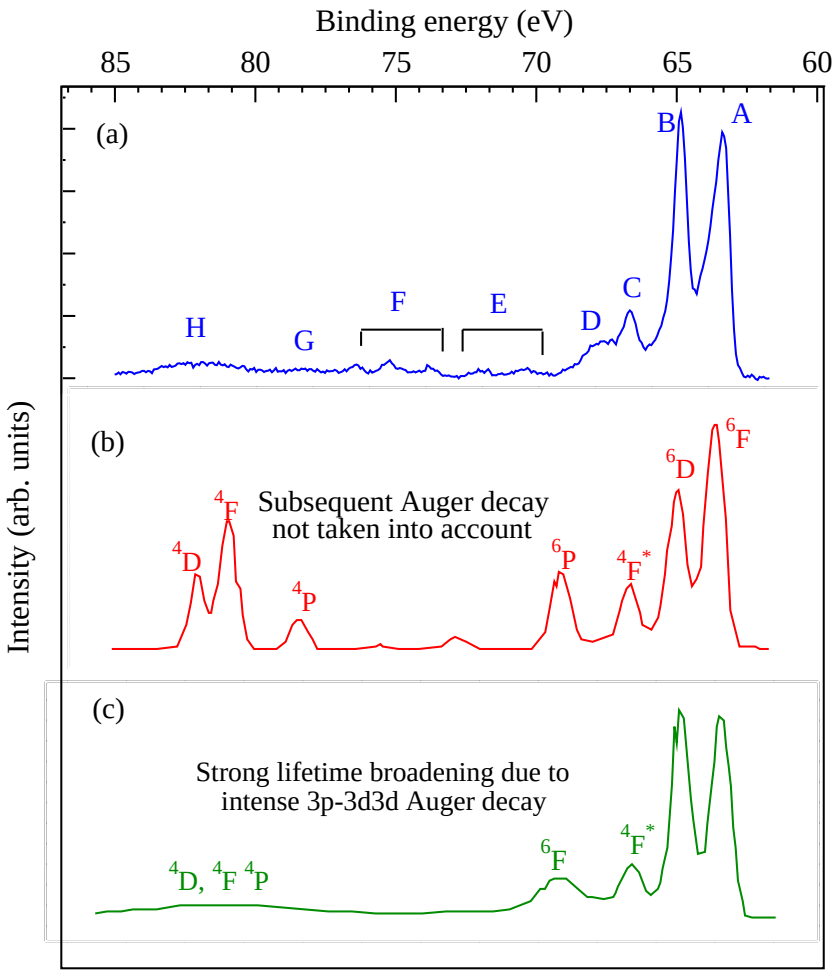

Figure 4.15: Fe $3p$ photoelectron spectra and results of the HF calculation taken from [85]: (a) experimental $3p$ photoelectron spectrum of atomic Fe, taken at photon energy of 127 eV. The peaks labelled by capital letters (see text) (b) and (c) show the calculated $3p$ *Fe* spectrum with and without concerning the subsequent Auger decay of the spectra respectively.

signal are suppressed as a result of the $3p^{-1} \rightarrow 3d3d$ SCK decay.

4.6.2 $3p$ photoelectron spectra of $FeCl_2$ and $FeBr_2$

Figure 4.16 shows in part (b) and (c) the experimental results of the molecular $3p$ photoelectron spectra of $FeCl_2$ and $FeBr_2$, whereas in the upper part (a) of the fig-

ure 4.16, atomic $3p$ photoelectron is presented. The $3p$ molecular $FeCl_2$ and $FeBr_2$ spectra have been taken at the photon energies of 100 eV and 120 eV respectively. The corresponding high photon flux of these photon energies were at the range of $1.1e^{14}$ photons/100 meV/s and at $1.5e^{14}$ photons/100 meV/s respectively. The monochromator and binding energy scale were calibrated using well-known photoelectron and Auger lines of Xenon [89]. All spectra were detected with the selected analyzer pass energy of 100 eV and corrected for the analyzer transmission.

In this section $3p$ molecular $FeCl_2$ and $FeBr_2$ spectra are compared with the data of the atomic Fe $3p$ photoelectron spectrum. Additionally by varying the halogen ligands of the Fe (here Cl and Br), influence of these halogens on the experimental spectra of the $FeCl_2$ and $FeBr_2$ are investigated.

In figure 4.16 (b) the $FeCl_2$ spectrum has two main regions which are labelled by I and II. Region I has two structures centered at the binding energy of 62.5 eV and 63.2 eV, whereas the region II contains two structures centered at the energies range 65.2 eV and 67.0 eV. From figure 4.15 (c) the $FeBr_2$ spectrum can be also classified into two regions I and II. In region I a main photoline and small feature appears at 62.0 eV and 62.3 eV. In region II features appear at the binding energies of 62.5 eV and 66.2 eV respectively.

The main photoline at the binding energy 62.0 eV of the molecular $FeBr_2$ differs slightly from the photoline at the binding energy 60.5 eV of the molecular $FeCl_2$, since the later is broader than that in $FeBr_2$. In addition the strong feature centered at the binding energy 64.5 eV of the molecular $FeBr_2$ appears clearly in contrast to the feature at the binding energy of 65.2 eV in the $FeCl_2$. This could refer to the sort of the ligands in the Fe, since chloride has a large electronegativity than bromide i.e. the two electrons in the $4s$ shell of the iron would be more attracted by chloride than in bromide.

Figure 4.17 displays the $3p$ and $2p$ photoelectron spectra in molecular $FeCl_2$ and the corresponding spectra in solids.

$3p$ and $2p$ X-ray photoelectron spectra (XPS) of $FeCl_2$ have been studied by Okusawa [90]. Okusawa suggested that the shoulder on the high binding energy

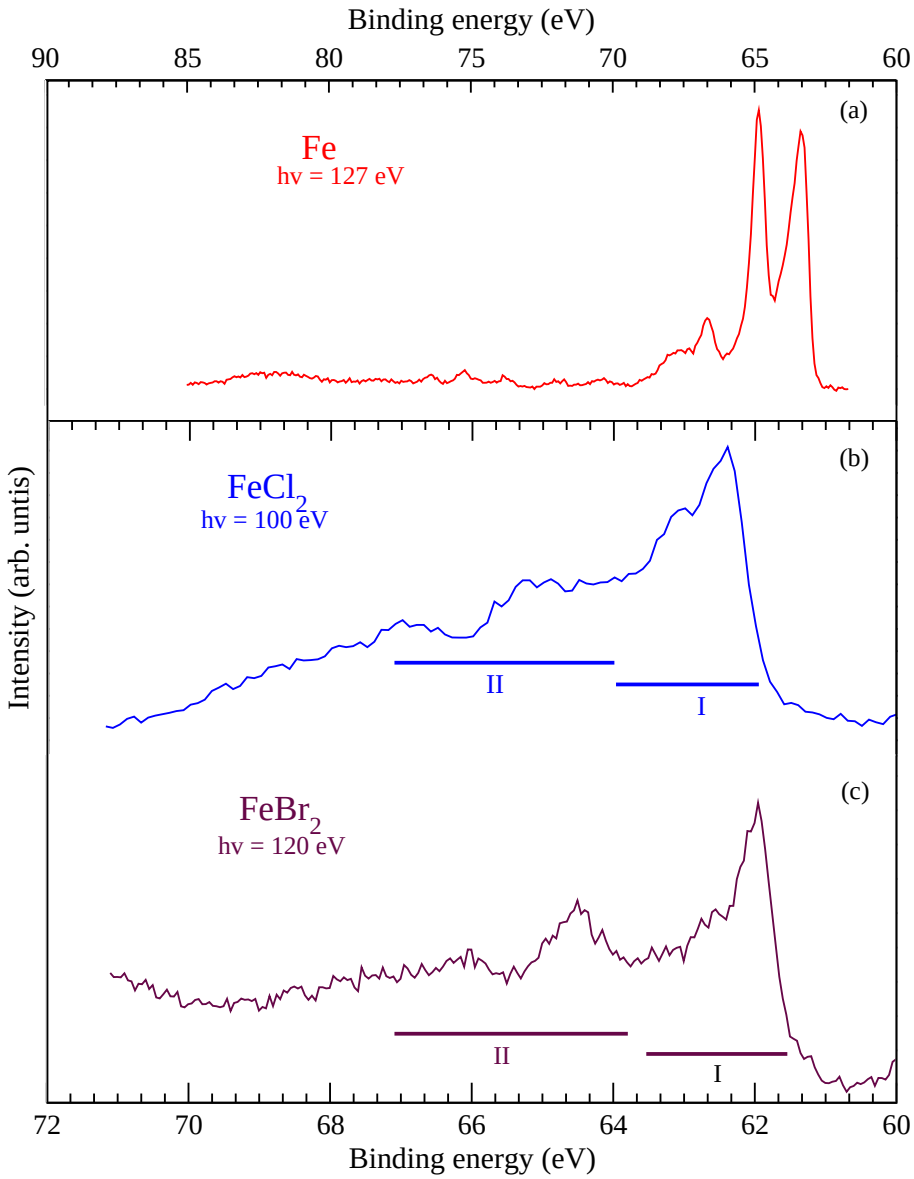

Figure 4.16: Comparison of the $3p$ atomic *Fe* and molecular $FeCl_2$ and $FeBr_2$ photoelectron spectra: upper part: experimental $3p$ photoelectron spectra of the atomic *Fe* at $h\nu$ = 127 eV taken from [85]. Panel (b) and (c) show the experimental results of the $3p$ molecular $FeCl_2$ and $FeBr_2$ taken at the photon energy 100 and 120 eV respectively. Two regions I and II of both spectra are shown (see the text).

side of the main line in the $3p$ $FeCl_2$ can be attribute to the spin-orbit splitting.

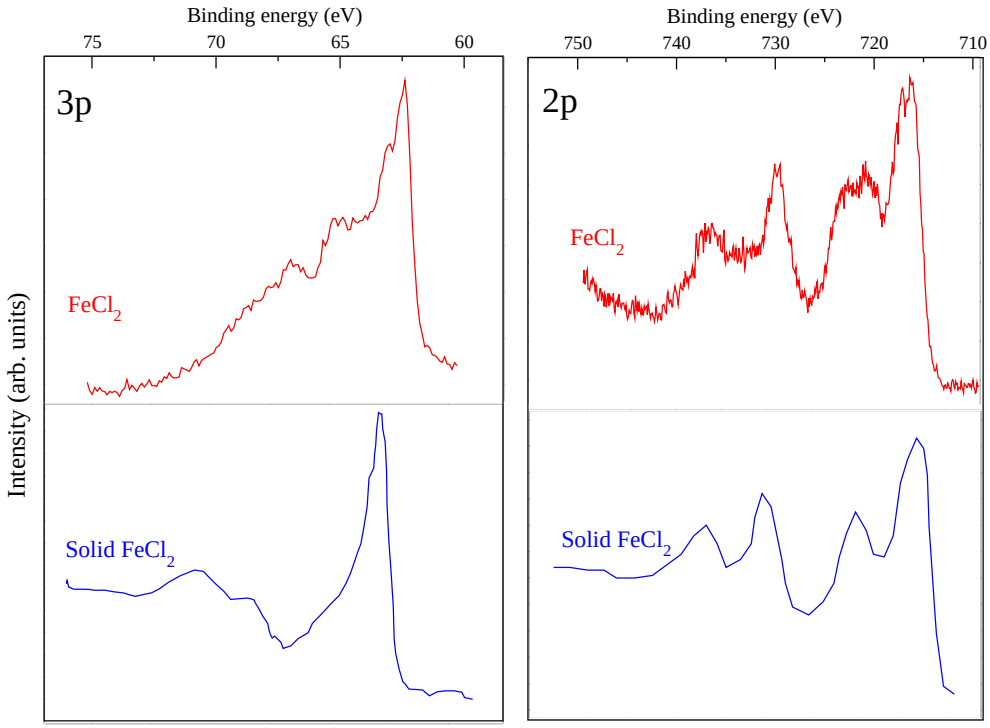

Figure 4.17: $FeCl_2$ $3p$, $2p$ photoelectron spectra and corresponding spectra in solid: experimental $3p$ $FeCl_2$ and $FeCl_2$ solid in the left panel compared with the $2p$ molecular $FeCl_2$ photoelectron spectra taken from [80] and its solid spectra in the right panel. Solid spectra of the $3p$ and $2p$ were taken from [90].

However it has been proved later that spin-orbit splitting is very small in the $3p$ to observe. Due to the larger $p-d$ interaction of the $3p$ hole, the multiplet splitting impacts the spectral shape more in the $3p$ spectrum than of the $2p$ hole. In contrast to the $2p$ spectrum, $3p$ spectrum is not separable into the main line and satellite. In [91] and [92] the multiplet line for the free V^{3+} and Cr^{3+} ions were calculated and they found that the multiplet lines spread over more 20 eV above the main line of these ions and the observed gross feature of the $3p$ XPS spectrum agree with these. This fact suggests that the effects of the change of the covalency induced by creation of a core hole is small for V^{3+} and Cr^{3+} ions [93].

K. Okada and A. Kotani [81] have successfully described the X-ray photoemission spectra (XPS) from the metal $2p$ core level in $FeCl_2$ using a charge transfer

model (CT). They considered a particular attention to the interplay between the intra-atomic multiplet coupling and covalency mixing effects. This result was successfuly consecutively applying of the CT model to explain the $2p$ photoelectron spectrum of the $FeCl_2$ in the gas phase [80]. This modeling based on the similarity of the solid $2p$ $FeCl_2$ spectrum with the molecular $2p$ $FeCl_2$. Despite the different characteristic of $3p$ multiplet nature in contrast to the $2p$ the CT modelling of the molecular $3p$ might be very useful to analyze the experimental spectrum.

4.7 $CoCl_2$

In this section $3p$ photoelectron spectra from $CoCl_2$ molecular is investigated. The purpose is to study the influence of the chloride ligand at the Co. The interaction of the $Co(3p)$ hole with the valence electrons is useful and can also be applied to study the influence of the inter-atomic interaction in the Co compound.

4.7.1 $3p$ photoelectron spectra of the atomic Co

Figure 4.18 (upper panel) shows the recorded experimental $3p$ photoelectron spectrum of atomic Co at 133.2 eV. At the low binding energy region two photolines are displayed, whereas several much weaker features at higher binding energies were observed. Hartree Fock (HF) calculations were carried out using the Cowan code for analyzing these structures.

The initial configurations $3p^6 3d^7 4s^2, 3p^6 3d^8 4s$ and $3p^6 3d^9$ and the final configurations $3p^5 3d^7 4s^2\ \varepsilon(s,d)$, $3p^5 3d^8 4s\ \varepsilon(s,d)$, $3p^5 3d^{10}\ \varepsilon(s,d)$ and $3p^5 3d^7 4p^2\ \varepsilon(s,d)$ were taken into account in the HF calculations, as well as the natural lifetime of the $3p^{-1}$ final state of the Co was considered by including the transition rates of the subsequent Auger decays in the calculations.

Calculated photoelectron spectra of the thermally populated initial fine-structure states Co ^4F_J are shown in figure 4.18 (lower panel). It presents the sum of several contributions of the initial fine-structure states ^4F_J that have been calculated

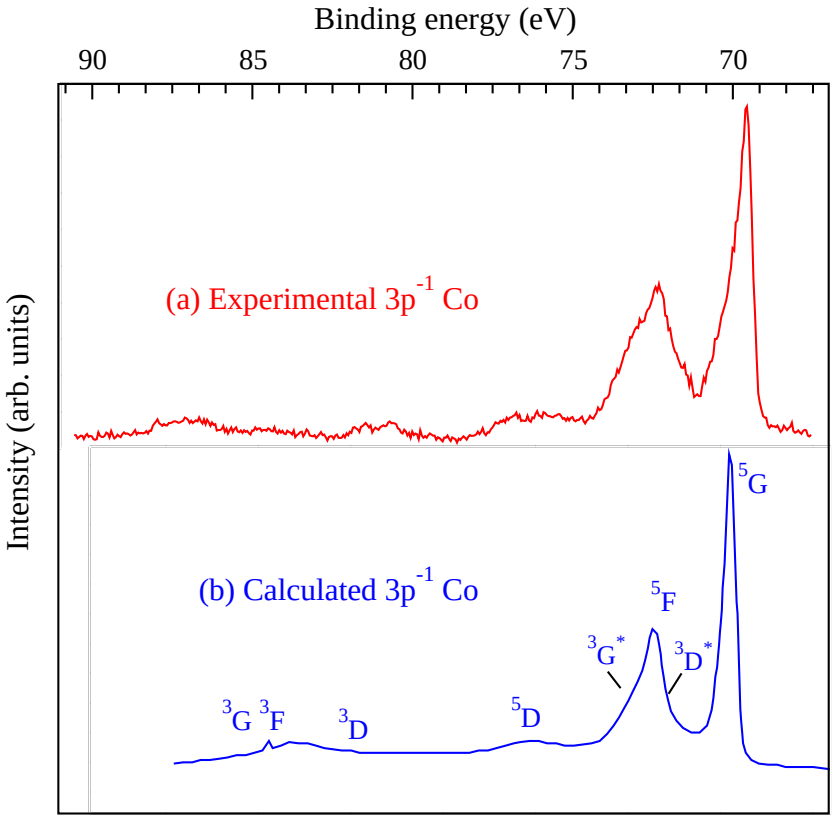

Figure 4.18: Co $3p$ photoelectron spectrum at hv = 133.2 eV and results of the Hartree Fock calculations taken from [85].

according to their thermal population at an evaporation temperature of 1800 K together with the relative line strengths of the transitions.

Similar to the $3p$ photoelectron spectra of atomic Fe, due to the strong $3p-3d$ interaction, HF calculations predict a large multiplet splitting of about 20 eV.

The $3p^{-1}$ multiplet structure consists of two energy regions: a low binding energy region where high-spin components ^5L were found and a high binding energy region where low spin-components ^3L were observed throughout the calculations.

These components are formed by parallel and anti-parallel coupling of the $3p^{-1}$ core hole states to the $3d^7\ ^4F$ parent term of the $3d$ subshell, respectively. $^3G^*$ and $^3D^*$ are two low spin components, which cause the asymmetry for the ^5F line, and they appear in the low binding energy as a result of parallel coupling of the $3p^{-1}$

core hole states to the re-coupled $3d^7\ ^2L^*$ parent term of the $3d$ subshell. Due to the subsequent Auger decay a line broadening of the low spin components, complete suppression of the photolines in the high energy region is noticed.

At the experimental binding energy 69.6 eV a distinctive line appear, which corresponds to the lowest $3p$ ionization threshold and can be ascribed to $3p^7 4s^2\ ^4F \rightarrow 3p^5 3d^7 4s^2\ ^5G$ transitions. The second main line at 72.3 eV originates form the ^5F state of the ion. The broad structure line at about 76 eV can be ascribed to $3d^7 4s^2\ ^4F \rightarrow 3p^5 3d^7 4s^2\ ^5D$ transitions. The weak structures at the energy range from 80 eV to 83 eV can be ascribed to $4d$ and $5s$ shakeup satellites of the main line ^5G. At the high energy range weak structures at about 87 eV can be attributed to the low-spin components ^3L. The very weak structure centered at 84 eV could not be reproduced by the HF calculations. However this structure maybe attributed to both the ^3D low spin and to the $4s$ and $5d$ shakeup lines of the second main line ^5F.

4.7.2 $3p$ photoelectron spectra of $CoCl_2$

Figure 4.19 (b) shows the experimental result of the $3p$ photoelectron spectrum of $CoCl_2$ in the binding energy range 65 eV to 85 eV. The spectrum was recorded at the photon energy of 130 eV, where the photon flux of this photon energy was at the range of $1.1e^{14}$ (photons/100 meV/s). The monochromator and binding energy scale were calibrated using well-known photoelectron and Auger lines of Xe [89]. All spectra were detected with the selected analyzer pass energy of 100 eV and corrected for the analyzer transmission. The resolution is 200 meV. The $3p$ photoelectron spectrum of $CoCl_2$ spectrum exhibits four structures labelled by A, B, C and D.

$3p$ photoelectron spectra of the molecular $CoCl_2$ can be classified here into two binding energy regions: a lower binding energy region with strong structures and a high binding energy region with less structured maxima.

The most pronounced photoline (A) of the $CoCl_2$ spectrum appears at the low binding energy of 67.5 eV. A weak structured peak is shown in structure (B) at the

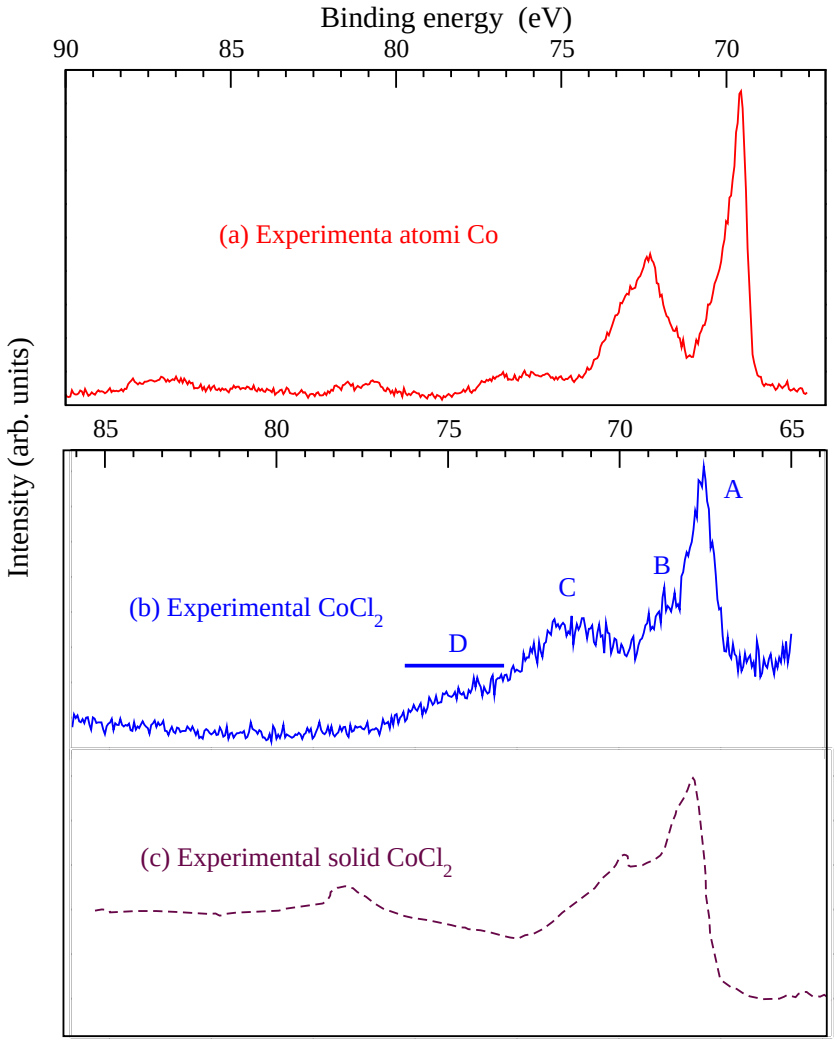

Figure 4.19: (a) $3p$ photoelectron spectra of Co taken at 133.2 eV [85], (b) molecular $CoCl_2$ at the photon energy of 130 eV and (c) $3p$ XPS $CoCl_2$ taken from [92].

binding energy of 69.0 eV, whereas an additional structure (C) is clearly centered at 71.0 eV. Less intense structure (D) ranges from 74.0 to 77.0 eV. At the high energy region there are no remarkable structures can be indicate. Figure 4.19 shows a comparison picture of the $3p$ molecular $CoCl_2$ spectra with the corresponding $3p$ atomic spectrum and the solid $CoCl_2$ spectrum. One can observe a kind of similarity in the main photoline (A) at 68 eV and the structure at the 72.0 eV of the

molecular $CoCl_2$ with the main photoline at 69.5 eV and the structure at 73 eV of the atomic Co.

According to a study of Ni $3p$-XPS in $NiCl_2$ [95]a significant difference in term of spectral shape between the applied CT model on $2p$ and $3p$ XPS TM compounds is presented. The experimental spectrum of $3p$-XPS $NiCl_2$ taken from [90] has been calculated by the CT model. CT acts between Ni $3d$ states and ligand $3p$ orbitals, the ground state can be described by a linear combination of $3d^8$, $3d^9\underline{L}$ and $3d^{10}\underline{L}^2$ electron configurations.

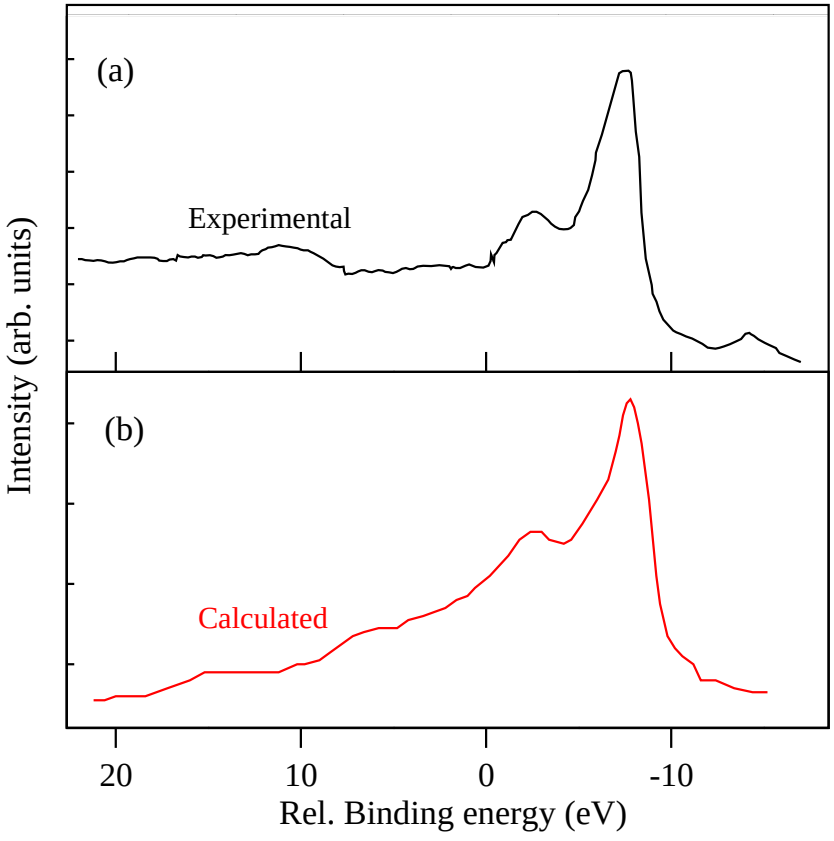

Figure 4.20: Experimental and theoretical Ni $3p$ XPS in $NiCl_2$. Upper panel: experimental data taken from [90]. Lower panel: theoretical spectrum obtained by convoluting the line spectrum by taking into account the multiplet-term dependence of life time. Theoretical data are taken from [95].

CT energy from the ligand state to the $3d$ levels is denoted by Δ. When a core hole is created, the energy differences are obtained by replacing Δ with $\Delta_f = \Delta - U_{dc}(3p)$, where $U_{dc}(3p)$ is the core-hole potential acting on $3d$ electrons.

OKADA et al. have calculated the Ni $3p$ XPS with a constant life time Γ for $NiCl_2$. This is shown in the upper part of Figure 4.21. Unsatisfied agreement between this theoretical result with the experimental result in Figure 4.20 (upper panel) appears. This has been improved by taking into account the *LS*-term dependence of the life time Γ^{-1} and hybridization effects and the effect of the core hole potential (U_dc)[94]. Figure 4.21 shows the U_{dc} dependence of Ni $3p$ XPS with fixed value of Δ. In the case of U_{dc} = 7.5 eV the second peak is fairly sharp and strong. By increasing U_{dc}, the $\underline{3p}3d^9\underline{L}$ final state become lower than the $\underline{3p}3d^8$, so that the character of the first peak is mainly the $\underline{3p}3d^9\underline{L}$ and that of the second one is the main peak in the free one.

Thus, the good agreement between the experimental $3p$-XPS and the calculated spectrum, which is obtained by convoluting the line spectrum using the *LS* term dependence of the life time (Γ^{-1}) confirms here the importance of the term dependence of Γ.

The reason why the term-dependent Γ is so important for TM $3p$ XPS is the following: in the case of the shallow core-level excitations, in general, the Slater integrals are larger than the spin-orbit splitting of the core hole states so that the *LS* scheme approximately describes the eigenstates of the systems. Since the Auger decay is due to the Coulomb interaction, there is no Auger matrix element between different *LS* eigenstates, giving strict selection rules for the Auger decay process. As a result we get the significant *LS*-term dependence of the life time, in other words, the final state dependence of the lifetime in the Ni $3p$ XPS. In the case of TM $2p$ XPS, the term dependence of the lifetime is averaged out because the large spin-orbit interaction of the $2p$ core mixes the *LS* states. Moreover decay processes other than the Coster-Kronig decay $(2p3d^8 \rightarrow 3d^6\ \varepsilon f)$ can contribute to the core-hole lifetime, so hat the energy dependence of Γ is much weakener.

From this investigation we can reflect this point also on our results in $FeCl_2$,

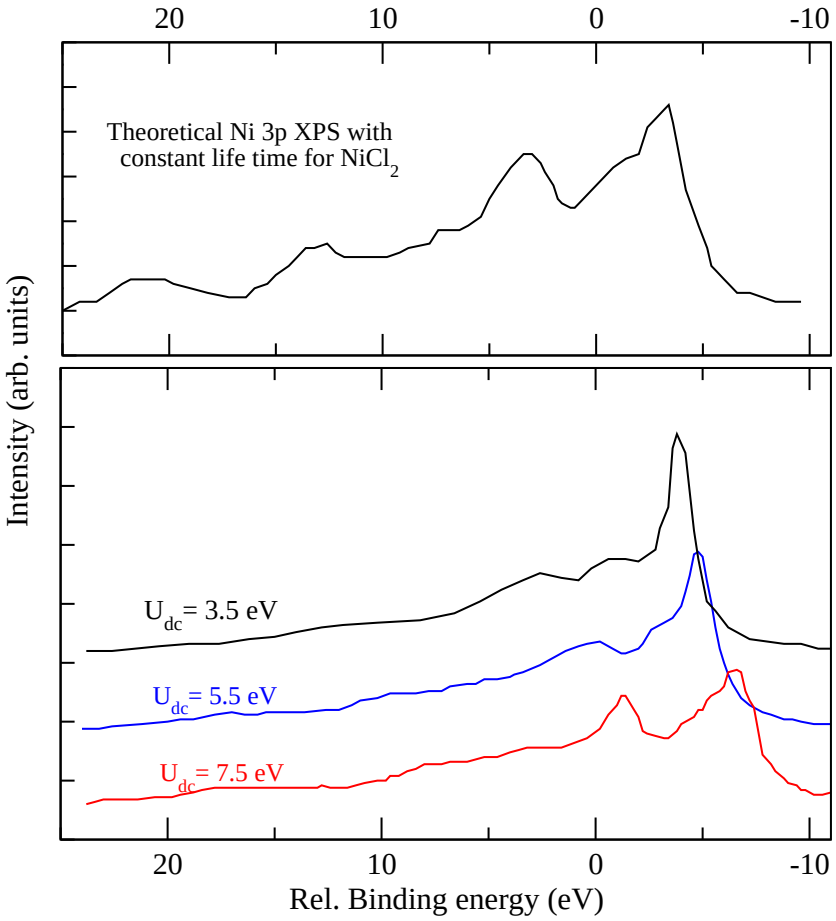

Figure 4.21: Dependence of the lifetime for $NiCl_2$ U_{dc} dependence. Upper panel: Theoretical Ni $3p$ XPS with constant lifetime for $NiCl_2$. Lower panel: U_{dc} dependence of Ni $3p$ XPS. The other parameter values are the same like those in the upper panel. These data are taken from [95].

$FeBr_2$ and $CoCl_2$. In other words, the successful using of the CT in $2p - FeCl_2$ is not enough to predict the modelling of our results without taking into account the properties of the TM $3p$-XPS i.e. the life term dependence.

Chapter 5

Summary

The work conducted for this thesis concerns the $3p$ core hole photoionization of the late $3d$-transition metal compounds, $FeCl_2$, $FeBr_2$ and $CoCl_2$ in the gas-phase. Photoabsorption and photoelectron spectra in the region of Fe and Co $3p$ excitation for the $FeCl_2$, $FeBr_2$ and $CoCl_2$ respectively are presented.

The emphasis of this work focused to describe the recorded data of the probed compounds in term of the different influences of the ligands (here Cl and Br), the differences between atomic and molecular spectra, the differences between the inner-shell excitation regions ($2p$ and $3p$ region) and finally in the terms of a comparison of the solid data with the corresponding molecular spectra.

$3p$ photoabsorption spectra of the $FeCl_2$, $FeBr_2$ and $CoCl_2$ show a degree of similarity when compared to the corresponding spectra of the Fe and Co respectively. The atomic data of $3p$ photoabsorption spectra are dominated by strong resonances. These are due to discrete transitions $3p^6 3d^N \rightarrow 3p^5 3d^{N+1}$ with a subsequent emission of electron $3p^5 3d^{N+1} \rightarrow 3p^6 3d^{N-2}\, \varepsilon(p,f)$. This is caused by the large overlap of the $3p$ and $3d$ wavefunctions.

The comparison of the $3p$ photoelectron spectra of $FeCl_2$, $FeBr_2$ and $CoCl_2$ with the corresponding $3p$ photoelectron spectra of the atomic Fe and Co respectively shows the more distinctive influence of the molecular binding on the valence electron. Since, the line structure of the photoelectron atomic spectra is governed

by the intensive multiplet splitting due to the Coulomb interaction of the $3p$ hole state with the $3d$ valence

A further investigation of the influence of the molecular binding on the valence electron was made through the comparison of the $3p$ with $2p$ photoelectron data of the $FeCl_2$. Contrary to the $2p$ photoelectron spectra of the $FeCl_2$, the $3p$ photoelectron of $FeCl_2$ provides a spectrum that is not separable into main line and satellites. This is a result of the large p-d interaction of the $3p$ hole. The charge transfer (CT) model has been applied successfully to the $2p$ photoelectron of the molecular $FeCl_2$ by introducing an additional $3d^7$ configuration. This suggests that the applied model of the solid $3p$ photoelectron spectra of the Ni in the $NiCl_2$ can be used as a model of the molecular $3p$ data by considering the $3p$ spectral shape properties which is affected by the life-time term dependence.

Bibliography

[1] H. F. Pen, J. van den Brink, D. I. Khomskii, and G. A. Sawatzky. Orbital Ordering in a Two-Dimensional Triangular Lattice Phys. Rev. lett. **78**, 1323 (1997).

[2] U. Werner und H. O. Lutz. *Wie moleküle "explodieren"*. Phys. Bl. **53**, 224 (1997).

[3] R. H. Dörner, J. M. Feagin, V. Mergel, O. Jagutzki, L. Spielberger, T. Vogt, H. Khemliche, M. H. Peior, J. Ullrich, C. L. Cocke, and H. Schmidt-Böcking. Photo-double-ionization of He: Fully differential and absoulte electronic and ionic momentum distribution, Phys. Rev. A **57**, 1074 (1998).

[4] Michael Martins. Core level photoionization of the transition metal atoms. Habilitationsschrift, Universität Hamburg, 2004.

[5] Jan M. Rost, K. Schultz, M. Domke, and G. Kaindl. Resonance parameters of photo doubly excited helium. J. Phys. B **30**, 4663 (1997).

[6] Volker Schmidt. Photoionization of atoms using synchrotron radiation. Rep. Prog. Phys. **55**, 1483 (1992).

[7] Volker Schmidt. Electron spectrometry of atoms using synchrotron radiation. Number 6 in Cambridge monographs on atomic, molecular and chemical physics. (Cambridge University Press, Cambridge, New York, 1997).

[8] C. D. Caldwell, M. O. Krause, R. D. Cowan, A. Menzel, S. B. Whitfield, S. Hallman, S. P. Frigo, and M. C. Severson. Inner-shell photoexcitation in an

open-shell atom: The Cl $2p \rightarrow ns, md$ spectrum as a case study. Phys. Rev. A **59**, 926 (1999).

[9] Björn Zimmermann. Vollstandig Experimente in der atomaren und molekularen Photoionsiation, PhD Thesis, TU-Berlin, 2000.

[10] S. Benzaid, M. O. Krause, A. Menzel, and C. D. Caldwell. Structure and dynamics of the $4p \rightarrow ns, md$ autoionizing resonances between the ^3p and ^1S thresholds in atomic bromine. Phys. Rev. A **57**, 4420 (2004).

[11] J. C. Salter. The theory of complex spectra. Phys. Rev. **34**, 1293 (1929).

[12] R. D. Cowan. The Theory of Atomic Structure and Spectra (University of California Press, Berkeley, 1981).

[13] I. Nenner and P. Morion. Electronic and nuclear relaxation of core-excited molecules. UVU and soft X-ray Photoionization. Edited by Uwe Becker and David A. Shirley. (Plenum Press, New York, 1996).

[14] T. Richter, K. Godehusen, M. Martins, T. Wolff, and P. Zimmermann. Interplay of Intra-atomic and Interatomic Effects: An Investigation of the *2p* core level spectra of atomic Fe and molecular $FeCl_2$ Phys. Rev. Lett. **93**, 023002 (2004).

[15] Frank de Groot. Multiplet effects in X-ray sepectroscopy. Coordination Chemistry Reviews. (In press).

[16] Takeo Jo and Akio Kotani. Narrowing due to valence mixing in the 3d core level spectra for Ce compounds. J. Phys. Soc. Jpn. **57**, 2288 (1988).

[17] O. Gunnarsson and K. Schönhammer. Electron spectroscopies for Ce compounds in the impurity model. Phys. Rev. B **28**, 4315 (1983).

[18] A. Fujimori and F. Minami. Valence-band photoemission and optical absorption in nickel compounds. Phys. Rev. B **30**, 957 (1984).

[19] G. A. Sawatzky and J. W. Allen. Magnitude and origin of the band gap in NiO. Phys. Rev. Lett. **53**, 2339 (1984).

[20] G. van der Laan, J. Zaanen, G. A. Sawatzky, R. Karnatak, J. M. Esteva. Comparison of X-ray absorption with X-ray photoemission of nickel dihalides and NiO. Phys. Rev. B **33**, 4253 (1986).

[21] J. Zaanen and G. A. Sawatzky, J. W. Allen. Band gaps and electronic structure of transition-metal compounds. Phys. Rev. Lett. **55**, 418 (1985).

[22] R. H. Potze and G. A. Sawatzky. Possibility for an intermediate-spin ground state in the charge-transfer material $SrCoO_3$. Phys. Rev. B **51**, 11501 (1995).

[23] Kozo Okada and Akio Kotani. Intersite screening effects in core-level spectra of low-dimensional copper compounds. Physica B **237**, 383 (1997).

[24] M. A. van Veenendaal and G. A. Sawatzky. Nonlocal screening effects in $2p$ x-ray photoemission spectroscopy core-level line shapes of transition metal compounds. Phys. Rev. Lett. **70**, 2459, (1993).

[25] F. Jollet, V. Ortiz and J. P. Crocombette. Influence of the band shapes in the Anderson impurity model. J. Electron Spectrosc. Relat. Phenomena **86**, 83 (1997).

[26] F. R. Edelr, A. M. Gurewitsch, R. V. Langmuir, and H. C Pollock. Radiation from electrons in a synchrotron. Phys. Rev. **71**, 829 (1947).

[27] F. R. Edelr, R. V. Langmuir, and H. C Pollock. Radiation from electrons accelerated in a synchrotron. Phys. Rev. **74**, 52 (1948).

[28] J. C. Salter. The self-cosistent field for molecules and solids. (McGraw hill, New York, 1974).

[29] R. P. Madden, and K. Codling. New autoionzing atomic energy levels in He, Ne and Ar. Phys. Rev. lett. **10**, 516 (1963).

[30] K. Wille. Synchrotron radiation sources, Rep. Prog. Phys. **54**, 10005 (1991).

[31] S. Hasimoto and S. Sasaki. Concept of a new undulator that will suppress the rational harmonics, Nucl. Instrum. Methods. **361**, 611 (1995).

[32] S. Sasaki, S. Hasimoto. H. Kobayashi. M. Takao, and Y. Miyahara. Conceptual design of quasiperiodic undulator. Rev. Sci. Instrum. **66**, 1953 (1995).

[33] M. Martins, G. Kanidl, and N. Schwenter. Design of high-resolution BUS XUV-beamline for BESSY II. J. Electron Spec. Ralat. Phenom. **101**, 956 (1999).

[34] R. Follath and F. Senf. First undulator beamlines in operation at BESSY II. SRN **12**, 34 (1999).

[35] H. A. Padmore. Optimization of soft x-ray monochromators. Rev. Sci. Instrum. **60**, 1608 (1989).

[36] H. A. Padmore, M. R. Howells, and W. R. McKinney. Techniques of Vacuum Ultraviolet Physics, chapter Grazing-Incidence Monochromators for third generation synchrotron radiation sources. Pages 1-49. (Academic Press, Orlando, F1, 1997).

[37] H. A. Padmore and T. Warwick. New developments in soft x-ray monochromators for third generation synchrotron radiation sourcs. J. Electron spectrosc. Relat. Phenom. **75**, 9, (1995).

[38] G. Kaindl, K. Schulz, P. A. Heimann, J. D. Bozek, and A. S. Schlachter. Ultra-high resolution in the soft X-ray region at beamline 9.0.1 at the ALS. SRN **8**, 29 (1995).

[39] K. Schulz, G. Kaindl, M. Domke, J. D. Bozek, P.A. Heimann, A. S. Schlachter and J. M. Rost. Observation of new rydberg series and resonances in doubly excited helium at ultrahigh resolution. Phys. Rev. Lett. **77**, 3086 (1996).

[40] M. Martins, G. Kaindl, N. Schwentner. Design of the high-resolution BUS XUV-beamline for BESSY II. J. Electron Spectrosc. Relat. Phenom. **101**, 965 (1999).

[41] R. Püttner. Status and future development of the U125/2-SGM. (Beamline report at BESSY II, 2004).

[42] H. A. Padmore. Optimization of soft X-ray monochromators. Rev. Sci. Instrum. **60**, 1608 (1989).

[43] William Burling Peatman. Grating, mirrors and slits. (Gordon and Breach Science Publishers. Amsterdam, The Netherlands, 1997).

[44] G. Scoles. Atomic and molecular beam methods. Vol. **1** ,(Oxford University Press, 1988).

[45] T. Hayaishi and P. Zimmermann. Ion yield spectroscopy with soft X-rays. Ch. 13, P. 465, UVU and soft X-ray Photionization, Edited by Uwe Becker and David A. Shirley, (Plenum Press, New York 1996).

[46] A. E. Cameron and D. F. Eggers, Jr. An Ion "Velocitron" Rev. Sci. Instrum. **19**, 605 (1948).

[47] W. C. Wiley and I.H. Mclaren. Rev. Sci. Instrum. **26**, 1150 (1955).

[48] U. Becker, D. Szostak, H.G. Kerkhoff, M. Kupsch, B. Langer, R. Wehlitz, A. Yagishita and M. Hayaishi. Subshell photoionization of Xe between 40 and 1000 eV. Phys. Rev. A **39**, 3902 (1989).

[49] P. Lablanquie and P. Morin. Double ionization following the $3d_{5/2}$ to 5p excitation in Kr. J. Phys. B **24**, 4349 (1991).

[50] Stefan Hüfner. Photoelectron Spectroscopy, volume 82 of Springer Series in Solid-states Sciences. (Springer, Berlin, Heidelberg, New York, 1995).

[51] J. Cooper and R. N. Zare. Angular disribution of photoelectrons. J. Chem. Phys. **48**, 942 (1968).

[52] A. Kotani, H. Ogasawara, K. Okada, B. T. Thole and G. A. Sawatzky. Theory of multiplet structure in $4d$ core photoabsorption spectra of CeO_2. Phys. Rev. **40**, 65 (1989).

[53] R. von Helmolt, J. Wecker, B. Holzapfel, L. Schultz, and K. Samwer. Giant negative magnetoresistance in perovskitelike $La_{2/3}\ Ba_{1/3}MnO_x$ ferromagnetic films. Phys. Rev. Lett. **71**, 2331 (1993).

[54] D. I. Khomskii and G. A. Sawatzky. ssc, **102**, 87 (1997).

[55] V. P. Spiridonov, A. G. Gershikov and V. S. Lyutsarev. Electron diffraction analysis of XY_2 and XY_3 molecules with large amplitude motion : Part I. Dynamical model and molecular scattering function V.P. Spiridonov. J. Mol. Struct. **221**, 57 (1990).

[56] M. Meyer, Th. Prescher, E. von Raven, M. Richter, E. Schmidt, B. Sonntag, and H. E. Wezel. In giant resonances in atoms, molecules, and solids, edited by J. P. Connerade, J. M. Esteva, and R. C. Karnatak (Plenum, New York, 1987); Z. Phys. D **2**, 347 (1986).

[57] Frederick H. Mies. Configuration interaction theory. Effects of overlapping resonances. Phys. Rev. **175**, 164 (1968).

[58] C. E. Moore, *Atomic Energy levels,* Natl. Bur. Stand (U.S.) Circ. No. 467 (U.S. GPO, Washington, DC, 1971).

[59] H. Feist, M. Feldt, Ch. Gerth, M. Martins, P. Sladeczek, and P. Zimmermann. $3p$-photoionization resonances of atomic Fe, Co, and Ni studied by the observation of singly and doubly charged photoions. Phys. Rev. A **53**, 760 (1996).

[60] J. T. Costello, E. T. Kennedy, B. F. Sonntag and C. W. Clark. $3p$ photoabsorption of free and bound Cr, Cr^+, Mn, and Mn^+ Phys. Rev. A **43**, 1441 (1991).

[61] F. M. F. de Groot. Differences between L_3 and L_2 X-ray absorption spectra Physica B **209**, 15 (1995).

[62] Z. Hu, H. von Lips, M. S. Golden, J. Fink, G. Kaindl, F. M. F de Groot, S. Ebbinghaus and A. Reller. Multiplet effects in the Ru $L_{2,3}$ X-ray-absorption spectra of Ru IV and Ru V compounds Phys. Rev. B **61**, 5262 (2000).

[63] L. C. Davis and L. A. Feldkamp. $M_{2,3}$ spectrum of atomic Mn Phys Rev. A **17**, 2012 (1987).

[64] Edwin Kukk, Marko Huttula, Jaume Rius i Riu, Helena Aksela and Seppo Aksela. Photoionization, photoexcitation and photofragmentation of caesium halide dimers. J. Phys. **37**, 2739 (2004).

[65] Vambola Kisand, Edwin Kukk, Marko Huttula, Arto Koivukangas, Helena Aksela, Ergo Nõmmiste and Seppo Aksela. Fragmentation and electronic decay of vacuum-ultraviolet-excited resonant states of molecular CsCl. J. Phys. B **36**,3909 (2003).

[66] F Von Busch. Extraction of representative kinetic energy parameters from photofragmentation time-of-flight spectra J. Phys. B Phys. **34**, 431 (1995).

[67] RD. Levine and RB. Bernstein. Molecular reaction dynamics and chemical reactivity. (Oxford university Press, New York, 1987).

[68] T. Bear and WL. Hase. Unimolecular reaction dynamics, theory and experiments. (Oxford university Press, New York, 1996).

[69] Walker Bleakney. The Ionization of hydrogen by single electron impact. Phys. Rev. **35**, 1180 (1930).

[70] Homer D. Hagstrum and John T. Tate. Ionization and dissociation of diatomic molecules by electron impact. Phys. Rev. **59**, 354 (1941).

[71] J. A. Hipple and E. U. Condon. Detection of metstable ions with the mass spectrometer. Phys. Rev. **68**, 54 (1945).

[72] J. A. Hipple, R. E. Fox, and E. U. Condon. Metastable ions formed by electron impact in hydrocarbon gases. Phys. Rev. **69**, 347 (1946).

[73] H. O. Folkerts, F. W. Bliek, M. C. de Jong, R. Hoekstra and R.Morgenstern. Dissociation of CO induced by ions: I. Fragmentation and kinetic energy release spectra. J. Phys. B **30**, 5833 (1997).

[74] R. l. Watson and R. J. Maurer. Nucl. Instrum. Methods A **262**, 99 (1987).

[75] Till Luhmann, *Ph.D. Thesis* TU-Berlin, Verlag Dr. Koester, 1995.

[76] Shun-ichi Nakai, Hiroo Nakamori, Akihiro Tomita, Kenjiro Tsutsumi Hatsuo Nakamura and Chikara Sugiura. Soft-x-ray $M_{2,3}$ absorption spectra of some transition-metal halides. Phys. Rev. B **9**, 1870 (1973).

[77] Paul S. Bagus, R. Broer, W. A. de Jong, W. C. Nieuwpoort, F. Parmigiani, and L. Sangaletti. Reply: Bagus et al. Phys. Rev. lett. **86** , 3693, (2001).

[78] P. S. Bagus, W. A. de Jong, W. C. Nieuwpoort, F. Parmigiani, and L. Sangaletti. Atomic many-body effects for the p-shell photoelectron spectra of transition metals. Phys. Rev. Lett. **84**, 2259 (2000).

[79] M. Taguchi, T. Uozumi, K. Okada, H. Odasawara, and A. Kotani. Comment on Atomic many-body effects for the p-shell photoelectron spectra of transition metalsPhys. Rev. Lett. **86**, 3692 (2001).

[80] T. Richter, K. Godehusen, M. Martins, T. Wolff, and P. Zimmermann. Intraatomic and Interatomic Effects: An Investigation of the $2p$ core level spectra of atomic Fe and molecular $FeCl_2$. Phys. Rev. Lett. **93**, 023002 (2004).

[81] Kozo Okada and Akio Kotani. Ineratomic and intra-atomic configuration interactions in core-level X-ray photoemission spectra of late transition-metal compounds. J. Phys. Soc. Jpn. **61**, 4619 (1992).

[82] Munetaka Taguchi, Takayuki Uozumi and Akio Kotani. Theory of X-ray photoemission and X-ray emission spectra in Mn compounds. J. Phys. Soc. Jpn. **66**, 247 (1997).

[83] J. Ullrich, R. Moshammer, R. Dörner, O. Jagutzki, V. Mergel, H. Schmidt-Böcking and L. Spielberger. Recoil-ion momentum spectroscopy. J. Phys. B **30**, 2917 (1997).

[84] R. Dörner, V. Mergel, O. Jagutzki, L. Spielberger, J. Ullrich, R. Moshammer and H. Schmidt-Böcking. Cold Target Recoil Ion Momentum Spectroscopy: a 'momentum microscope' to view atomic collision dynamics. Physics Reports. **330**, 95 (2000).

[85] K. Tiedtke, Ch. Gerth, M. Martins and P. Zimmermann. Term-dependent lifetime broadening in the $3p$ photoelectron spectra of atomic Fe and Co. Phys. Rev. A **64**, 022705 (2001).

[86] E. Schmidt, H. Schröder, B. Sonntag, H. Voss, and H. E. Wetzel. $M_{2,3}$-shell Auger and autoionisation spectra of free Cr, Mn, Fe, Co, Ni and Cu atoms. J. Phys. B **17**, 707 (1984).

[87] Ch. Gerth, K. Tiedtke, M. Martins, B. Obst, P. Zimmermann, P. Glatzel, A. Verweyen, Ph. Wernet and B. Sonntag. Valence satellite and $3p$ photoelectron spectra of atomic Fe and Cu. J. Phys. B **31**, 2539 (1998).

[88] Eugene McGuire. Multiplet effects on the widths of photoelectron peaks. Phys. Rev. A **10**, 32 (1974).

[89] L. O. Werme, T. Bergmark and K. Siegbahn. The high resolution $L_{2,3}$ MM and $M_{4,5}$ NN auger spectra from Krypton and $M_{4,5}$ NN and $N_{4,5}$ 00 Auger spectra from Xenon. Physica Scripta **6**, 141 (1972).

[90] M. Okusawa. Splitting of core-level XPS lines of transition-metal ions in compounds and moment of the lines. Phys. stat. sol.(b). **124**, 673 (1984).

[91] Tsuyoshi Yamaguchi and Satoru Sugano. Multiplet structure in X-ray 3p-shell photoelectron spectra of chromium compounds. J. Phys. Soc. Jpn. **42**, 1949 (1977).

[92] M. Okusawa, K. Tsutsumi, T. Ishii and T. Sagawa. Splitting of $3p$ spectra of transition-metal ions in X-ray photoemission of VCl_3, $CrCl_3$ and $CrBr_3$. J. Phys. Soc. Jpn. **51**, 510 (1982).

[93] Susumu Asada and Satoru Sugano. Satellites in X-ray photoelectron spectra of transition-metal compounds. J. Phys. Soc. Jpn. **41**, 1291 (1976).

[94] G. Lee and S.-J. Oh. Electronic structures of NiO, CoO, and FeO studied by $2p$ core-level X-ray photoelectron spectroscopy. Phys. Rev. B **43**, 14674 (1991).

[95] K. Okada, A. Kotani, H. Ogasawara, Y. Seino and B. T. Thole. Auger decay of quasiparticle states: Calculation of the Ni $3p$ photoemission spectrum in $NiCl_2$. Phys. Rev. B **47**, 6203 (1993).

Eidesstattliche Versicherung

Ich versichere hiermit, daß ich diese Arbeit selbständig verfaßt und keine anderen als die angegebenen Hilfsmittel verwendet habe.

Berlin

Oktober 2005

MOHAMED AL-HADA